BioNanoScience (2022) 12:927–945
https://doi.org/10.1007/s12668-022-00990-2

Current Flow in a Cylindrical Nanopore with an Object–Implications for Virus Sensing

Mohammad Tajparast[1] · **Mladen Glavinovic**[2]

Accepted: 2 May 2022 / Published online: 19 May 2022

Abstract

Interest is growing in nanopores as real-time, low-cost, label-free virus size sensors. To optimize their performance, we evaluate how external electric field and ion concentrations and pore wall charges influence currents and object (disk) radius-current relationship using simulations. The physics was described using the Poisson-Nernst-Planck and Navier–Stokes equations. In a charged cylindrical nanopore with a charged disk, elevated external electric field produces higher (and polarity independent) ion concentrations and greater ion current (largely migratory). Elevated external ion concentrations also lead to higher concentrations (mainly away from the pore wall), greater axial electric field especially in the disk-pore wall space, and finally larger current. At low concentrations, current is disk radius independent. The current rises as concentrations increase. Interestingly, the rise is greater for larger disks (except when the pore is blocked mechanically). Smaller cross-sectional area for current flow or volume exclusion of electrolyte by object thus cannot be universally accepted as explanations of current blockage. Ion current rises when pore wall charge density increases, but its direction is independent of charge sign. Current-disk radius relationship is also independent of pore wall charge sign. If the pore wall and disk charges have the same sign, larger current with bigger disk is due to higher counter-ion accumulation in the object-pore wall space. However, if their signs are opposite, it is largely due to elevated axial electric field in the object-pore wall space. Finally in uncharged nanopores, current diminishes when disk radius increases making them better sensors of virus size.

Keywords Virus detection · Ion current · Pathogens · Cylindrical nanopore · Poisson-Nernst-Planck · Navier–Stokes

1 Introduction

Micropores have been used for a long time for rapid estimation of cell numbers, size, and "dwell time" (Coulter counter; [1, 2]). Interest in using pores as low-cost, rapid, and label-free estimators of properties of pathogens (such as viruses) is large and growing. However, viruses are smaller than cells and vary in size greatly (from several to several hundred nanometers [3]). Estimating their size–an important descriptor in their classification [4]–thus often requires nanopores. We classify the pore size on a logarithmic scale (with base 10; [5]). If the pore size ranges from 0.1 to 100 nm, it is considered a nanopore, and if it ranges from 0.1 to 100 µm, it is considered a micropore [5]. Nanopores are already used as sensors of single molecules–DNA [6–9], proteins [10–12], peptides [13, 14], and amino acids [15, 16], and solid-state nanopores as diagnostic tools for infectious diseases [17].

In all cases, the "object" size is estimated from a transient and discrete ionic current blockage during its translocation through the pore–the larger the object (and the smaller the cross-sectional area for current flow) the larger the current blockage. This "resistive-pulse method" [18] based on the size-exclusion principle [2] can also yield the shape of objects if pores with irregularities (a pore is considered irregular if its radius changes axially) are used [19, 20]. When an object passes through a pore, it often rotates. If the object is non-spherical, the cross-sectional area for the current flow changes and this leads to current fluctuations that contain information about how non-spherical the object is [21]. When a spherical object rotates, the cross-sectional area for the current flow does not change. Although this method is

---

✉ Mladen Glavinovic
mladen.glavinovic@mcgill.ca

[1] Department of Civil Engineering and Applied Mechanics, McGill University, Montreal, PQ, Canada

[2] Department of Physiology, McGill University, 3655 Sir William Osler Promenade, Montreal, P.Q. H3G 1Y6, Canada

now used for size and shape characterization of larger viruses [4, 20, 22, 23], it is unclear whether it would be suitable for characterization of smaller viruses using nanopores. However, shape is a powerful descriptor of viruses that vary in their shape greatly and can be globular (coronaviruses), oval shaped (poxviruses), rod-like (as many plant viruses), or head and tail like (bacteriophages) [24].

What is critically important is to understand the relationship between the cross-sectional area for current flow and current. Presently, the "size-exclusion principle" is the most widely held view. Expanding on this notion, it has been argued that the volume exclusion of electrolyte solution by the object also contributes to the current decrease during its translocation [25, 26]. In this study, we challenge these notions as a general explanation of current blockage because ions are as a rule not uniformly distributed within charged pores. Screening charges formed to counterbalance surface charges are concentrated near the pore wall [27–29]. Given such charges' distribution, the current-object size dependence cannot be one of progressive linear decrease, but it is unclear what the relationship is, and what influences it.

The object if charged also induces screening charges within nanopore. It has been suggested that this leads to larger current, partially counterbalancing the current decrease caused by smaller cross-sectional area for current flow and volume exclusion of electrolyte solution by the object, finally producing multi-level current changes [26]. This is an interesting, but a simplistic proposition because charged disk surfaces that may induce such currents will also largely block them mechanically. However, a charged object will affect the electric field (both its radial and axial components) within the nanopore (especially if the disk and the pore wall are charged differently). The radial electric field controls the radial migratory current around the disk and may change the overall axial migratory current in the disk-pore wall space, but it is unclear how and how much. Finally, even an uncharged object changes the electrostatics (and thus electro-kinetics) within the nanopore because it is a low permittivity material ($\varepsilon_{r,d} = 2$; [30]) within a highly polarizable core of the nanopore ($\varepsilon_{r,w} = 80$; [30]).

The presence of two charged surfaces in close proximity can change ion currents and conductivity greatly. Even a "simple" charge non-uniformity at the pore walls can lead to pronounced changes of ion fluxes [31], pore conductance [32], and current rectification [27, 32–35]. In engineering, such nanopores are used as ionic diodes and transistors [36–39] or serve as ion filters [29]. A systematic evaluation of how external factors and pore parameters influence the current in a charged cylindrical nanopore with a charged disk is clearly needed.

We evaluate how external electric field and ion concentrations and pore wall charges influence ion currents and disk radius-current relationship. The transport of K^+ and Cl^- was simulated using the Poisson–Nernst–Planck (PNP) equations [40] and was coupled to the transport of water using the Navier–Stokes (NS) equation [41, 42]. The electrostatic-electro-kinetic-hydrodynamic variables (potential, mobile charge density and ion currents) were subsequently evaluated.

2 Methods

2.1 Geometry of Simulation Domain, Parameters, Constants, and Boundary Conditions

Figure 1 gives the simulation space which consists of a cylindrical nanopore, two compartments flanking the nanopore, and a piece of membrane separating the compartments. All subdomains and boundaries are enumerated, and their dimensions are given (Fig. 1A). Figure 1B depicts meshing of the simulation space and Fig. 1C shows its 3D representation. Table 1 lists the electrostatics, electro-kinetics, and fluidics boundary conditions implemented in this study and Table 2 details the parameters and physical constants used. Note that the Poisson equation (i.e., electrostatics) was implemented in all subdomains, whereas the Nernst-Planck equation (i.e., electro-kinetics) and the Navier–Stokes equation (i.e., hydrodynamics) were only defined in subdomain 1 (i.e., electrolyte solution). The finite element method system was used to solve coupled PNP-NS equations (see below). In all simulations, diffusion constants of ions (K^+ and Cl^-) are known [56], but it is not so clear what the values may be in the confined space of the nanopore, where the electrostatic and non-electrostatic interactions with its walls [54] restrict their movement. To simplify the computation, we assumed that both diffusion constants (but also the dielectric constant of water and its viscosity) are homogeneous, isotropic, and the same as in the aqueous solution.

2.2 General Formulation of Mathematical Simulations

We used the Nernst-Planck equation to calculate ionic fluxes within a nanopore for both K^+ and Cl^- ions. The Poisson equation was used to compute the electric potential (ψ) due to mobile charges (inside the nanopore and in two compartments flanking it) and fixed charges (on the pore and disk walls; Eq. (1)), while the Laplace's equation (Eq. (2) calculates the electric potential (ϕ) due to applied external electric field (i.e., the potential difference between the upper and lower controlling edges) as follows:

$$-\nabla \bullet \varepsilon_0 \varepsilon_r \nabla \psi = \rho_e \tag{1}$$

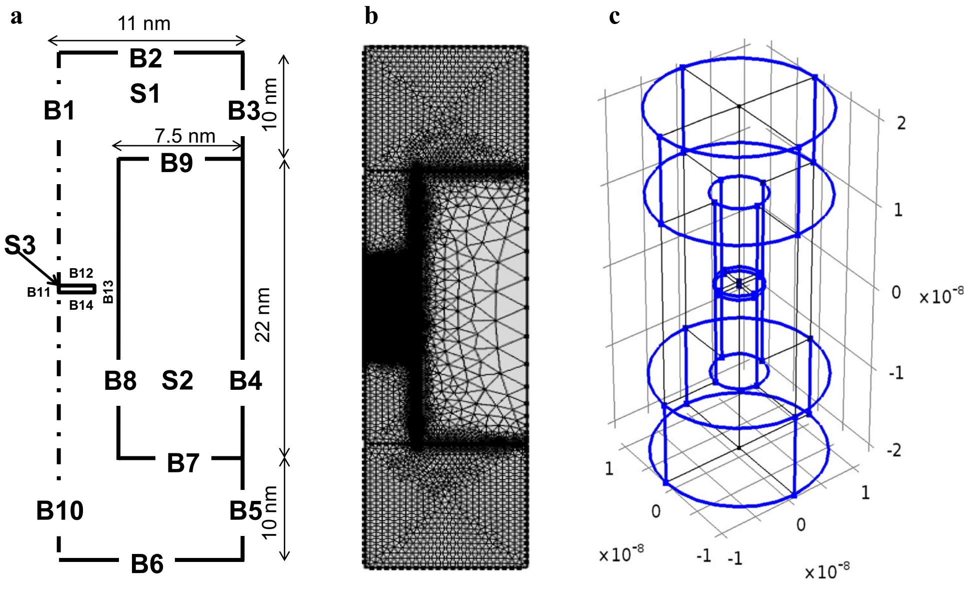

Fig. 1 Model geometry. **a** Hemi-section of the simulation space consisting of 3 subdomains–a cylindrical nanopore, one compartment on each side and a membrane patch separating them. In total, the model has 14 boundaries. Disk was positioned 1.5 nm above the nanopore center; its thickness was 0.5 nm, whereas its radius (r_o; subdomain S3) ranged from 0.5 to 3.25 nm. Radius of cylindrical nanopore was 3.5 nm. Other dimensions are given on the figure. The 3D-model is generated by the rotation of the hemi-section about central axis by 360°. All boundary conditions are given in Table 1. **b** Simulation space meshing. **c** 3D representation of the simulation space

Table 1 Boundary conditions

Boundary	Hydrodynamics	Electrostatics (Poisson's eqn.)	Electrostatics (Laplace's eqn.)	Electro-kinetics
B1, B10	Axial symmetry	Axial symmetry	Axial symmetry	Axial symmetry
B2 and B3	Pressure ($p_u = 0$ Pa); no viscous stress	Electric potential V_u (0 V)	Electric potential V_u (as specified)	K^+-Cl^- (400 mM or as specified)
B4	Not applicable (not in contact with water; NS equation does not apply)	Zero charge symmetry (i.e., n·**D** = 0, D is an electrical displacement vector)[a]	Zero charge symmetry (i.e., n·**D** = 0, D is an electrical displacement vector)[a]	Not applicable (not in contact with liquid electrolyte; PNP equations do not apply)
B5 and B6	Pressure ($p_d = 0$ Pa); No viscous stress	Electric potential V_d (0 V)	Electric potential V_d (0 V)	K^+-Cl^- (400 mM or as specified)
B7 and B9	No slip	Surface charge density $\sigma = 0$ C/m^2	Not applicable[b]	No flux
B8	No slip	Surface charge density σ_w	Not applicable[b]	No flux
B11	Not applicable (not in contact with water; NS equation does not apply)	Axial symmetry	Axial symmetry	Not applicable (not in contact with liquid electrolyte; PNP equations do not apply)
B12-B14	No slip	Surface charge density σ_o	Not applicable[b]	No flux

[a] Zero charge symmetry (i.e., n·D = 0) signifies that the normal component of the electric displacement on a given boundary is zero and that there is only a tangential component. Note that D = ε0E + P, where ε0 is permittivity of vacuum, E is electric field and P is polarization

[b] Laplace's equation ($\nabla^2\phi = 0$) calculates the electric potential (ϕ) due to external electric field. The electric field due to charges (mobile or fixed) is not considered, and relative permittivities play no role. To solve this equation for ϕ, the external electric fields at the upper and lower boundaries (i.e., B2, B3, B5, and B6) are defined, whereas the electric potentials at the internal boundaries (i.e., B7, B8, B9, and B12-B14) are not required. No boundaries effectively exist there when solving Laplace's equation

$$\nabla^2\phi = 0 \tag{2}$$

where ε_0 is the permittivity of vacuum, ε_r is the relative dielectric constant of a chosen subdomain (as shown in Fig. 1 there are three subdomains in the model; their ε_rs are given in Table 2), and ∇ is the gradient operator. The charge density ρ_e (mobile) was calculated as follows:

Table 2 Model parameters and physical constants

Params	Values	Unit	Description	Refs
T	300.0	K	Temperature	
R	8.314	J/(mol·K)	Universal gas constant	[30]
e	1.602×10^{-19}	C	Elementary charge	[30]
D_K	1.960×10^{-9}	m^2/s	Diffusion coefficient of K$^+$ ions	[56]
D_{Cl}	2.030×10^{-9}	m^2/s	Diffusion coefficient of Cl$^-$ ions	[56]
ρ	1.0×10^3	kg/m^3	Fluid density	[30]
μ	1.0×10^{-3}	Pa s	Fluid viscosity	[30]
ε_0	8.854×10^{-12}	F/m	Permittivity of vacuum	[30]
$\varepsilon_{r,w}$	80.0	Dimensionless	Relative permittivity of water	[30]
$\varepsilon_{r,m}$	2.0	Dimensionless	Relative permittivity of membrane	[30]
$\varepsilon_{r,d}$	2.0	Dimensionless	Relative permittivity of object (disk)	[30]

$$\rho_e = F\sum z_a c_a \left(= e\sum z_a n_a\right) \tag{3}$$

Note that c_a is the molar concentration of each ion in [mol/m^3], z_a is the valence of ion a, n_a is the number density of ion a, and F is the Faraday constant (9.648×10^4 C/mol). The contribution of fixed charges (σ_w–pore wall charge density and σ_o–disk charge density) is included through electrostatic boundary conditions (Table 1). The International System of Units (SI) is used in all simulations, and mol/m^3 thus equals to mmol/liter (or simply mM).

The movement (convection–diffusion-migration) of ions in the electrolytic fluid was defined by the Nernst-Planck equation as follows:

$$\mathbf{J_a} = \mathbf{u}c_a - D_a\nabla c_a - m_a z_a F c_a \nabla\Phi \tag{4}$$

where $\mathbf{J_a}$ is the molar flux in mol/(m^2·s), whereas $\mathbf{u}$ denotes the fluid velocity calculated by the NS equation. D_a and m_a represent diffusivity and mobility of ion a, which are related by $m_a = D_a/(RT)$. R and T account for the universal gas constant ($R = 8.314$ J/(mol·K)) and absolute temperature in Kelvin, respectively. Finally, Φ denotes the total electric potential, which is the sum of ϕ and ψ.

Equation (5) gives the conservation of ionic mass in a steady-state situation.

$$\nabla \bullet \boldsymbol{J_a} = 0 \tag{5}$$

The Navier–Stokes equation (at steady-state condition), in the presence of external forces, was applied to model fluid velocity as follows:

$$\rho(\boldsymbol{u} \bullet \nabla\boldsymbol{u}) = -\nabla p + \nabla \bullet \left[\mu\left[\nabla\boldsymbol{u} + (\nabla\boldsymbol{u})^T\right]\right] + \boldsymbol{F_e} \tag{6}$$

$$\nabla \bullet \boldsymbol{u} = 0 \tag{7}$$

Equation (6) describes the conservation of momentum, whereas Eq. (7) accounts for the conservation of mass. The ρ, μ, and p stand for fluid density, viscosity, and pressure (defined as the isotropic part of the fluidic stress tensor), respectively. The vector $\mathbf{u}$ denotes the fluid velocity. Finally, $\mathbf{F_e}$ accounts for the electric force per unit volume, calculated as $\mathbf{F_e} = -\rho_e\nabla\Phi$.

At nanoscales, the Reynolds number is expected to be very low and fluid flow laminar with negligible inertial effects [43]. Indeed, we find that the Reynolds number is < 0.01, even for the highest water velocity within the nanopore (i.e., very low ensuring that the flow is laminar). Moreover, the nanopore size and the Debye length [44] are comparable. We thus used no-slip condition in all simulations, but a slip condition may be a better choice when the surfaces are strongly hydrophobic. Finally, our choice of a no-slip boundary condition enables us to resolve the flow inside the electric double layer.

2.3 Mathematical Model in the Cylindrical Coordinate System

This study uses the cylindrical coordinate system (the 2D r-z plane). The simplified Navier–Stokes equation (note that the velocity and its gradient in the θ–direction are ignored, and there is an axial symmetry in the z–direction) in terms of components of the stress tensor $\boldsymbol{\tau}$ are thus as follows:

$$r - \text{component}: \rho\left(u\frac{\partial u}{\partial r} + v\frac{\partial u}{\partial z}\right) = -\frac{\partial p}{\partial r} - \left[\frac{1}{r}\frac{\partial}{\partial r}(r\tau_{rr}) + \frac{\partial \tau_{rz}}{\partial z}\right] + F_{e-r} \tag{8}$$

$$z - \text{component}: \rho\left(u\frac{\partial v}{\partial r} + v\frac{\partial v}{\partial z}\right) = -\frac{\partial p}{\partial z} - \left[\frac{1}{r}\frac{\partial}{\partial r}(r\tau_{rz}) + \frac{\partial \tau_{zz}}{\partial z}\right] + F_{e-z} \tag{9}$$

The u and v are the r- and z-components of the fluid velocity, respectively. The τ_{ij} are the ij-th components of the viscous stress tensor $\boldsymbol{\tau}$**,** which for the Newtonian fluids in 2D r-z plane (in the cylindrical coordinate system) are defined as:

$$\tau_{rr} = -\mu\left[2\frac{\partial u}{\partial r} - \frac{2}{3}(\nabla \bullet \boldsymbol{u})\right] \tag{10}$$

$$\tau_{zz} = -\mu\left[2\frac{\partial v}{\partial z} - \frac{2}{3}(\nabla \bullet \boldsymbol{u})\right] \tag{11}$$

$$\tau_{rz} = -\mu\left[\frac{\partial v}{\partial r} + \frac{\partial u}{\partial z}\right] \tag{12}$$

$$\text{where} \nabla \bullet \boldsymbol{u} = \frac{1}{r}\frac{\partial}{\partial r}(ru) + \frac{\partial v}{\partial z} \tag{13}$$

The electrostatic force is defined as $\mathbf{F_e} = -\rho_e \nabla\Phi$, whereas the gradient operator in the cylindrical coordinate system is given by:

$$[\nabla\Phi]_r = \frac{\partial\Phi}{\partial r},\ [\nabla\Phi]_z = \frac{\partial\Phi}{\partial z} \tag{14}$$

When the components of the stress tensor (given in Eqs. (10)–(14)) are substituted into Eqs. (8) and (9) with constants ρ and μ, we obtain Eqs. (15) and (16) describing the Navier–Stokes equation in terms of velocity gradients.

$$r - \text{component}\ :\ \rho\left(u\frac{\partial u}{\partial r} + v\frac{\partial u}{\partial z}\right) = -\frac{\partial p}{\partial r} + \mu\left[\frac{\partial}{\partial r}\left(\frac{1}{r}\frac{\partial}{\partial r}(ru)\right) + \frac{\partial^2 u}{\partial z^2}\right] - \rho_e\frac{\partial\Phi}{\partial r} \tag{15}$$

$$z - \text{component}\ :\ \rho\left(u\frac{\partial v}{\partial r} + v\frac{\partial v}{\partial z}\right) = -\frac{\partial p}{\partial z} + \mu\left[\frac{1}{r}\frac{\partial}{\partial r}\left(r\frac{\partial v}{\partial r}\right) + \frac{\partial^2 v}{\partial z^2}\right] - \rho_e\frac{\partial\Phi}{\partial z} \tag{16}$$

Finally, note that the divergence operator in Eqs. (1) and (5) is defined as:

$$\nabla \bullet \boldsymbol{J} = \frac{1}{r}\frac{\partial}{\partial r}\left(rJ_r\right) + \frac{\partial J_z}{\partial z} \tag{17}$$

The J_r and J_z are the r- and z- components of vector $\mathbf{J}$.

The system of coupled PNP and NS equations was solved using a finite element method based on a commercial software package COMSOL Multiphysics 4.3 (COMSOL, Burlington, MA, USA), whereas the postprocessing was performed using a MATLAB software package for scientific and engineering computation (MathWorks, Natick, MA, USA).

3 Results

3.1 Effect of External Electric Field on Ion Currents in a Charged Nanopore with a Charged Disk

The color-coded 2D distributions shown on top depict the effect of external axial electric field (E_{ex}) on the axial electric field (E_{ax}), K^+ and Cl^- concentrations ($\mathrm{co_K}$ and $\mathrm{co_{Cl}}$) within the nanopore (Fig. 2). To test whether the mesh sizes are adequately small (note that the mesh size differs depending on the location and is smaller near the disk and close to the edges; Fig. 1), we made some simulations where size was 100% bigger. In each set of 2D distributions, the results with double size mesh are shown as third panels (their V_u was +1 V). This change did not affect the 2D distributions of the E_ax, $\mathrm{co_K}$, and $\mathrm{co_{Cl}}$ (Fig. 2). Mesh size is thus adequately fine.

Radial profiles of the E_ax, $\mathrm{co_K}$, and $\mathrm{co_{Cl}}$ above the object-disk (at $z = 4$ nm which is indicated by the upper horizontal line; $E_\mathrm{ax,u}$, $\mathrm{co_{K,u}}$ and $\mathrm{co_{Cl,u}}$) and in the disk-pore wall space (at the disk's axial mid-point; i.e., at $z = 1.5$ nm; $E_\mathrm{ax,o}$, $\mathrm{co_{K,o}}$ and $\mathrm{co_{Cl,o}}$), which are critical for understanding how current is generated and controlled, are also shown. Lower horizontal line depicts the axial midpoint (i.e., $z = 0$ nm). The $\mathrm{co_{K,u}}$ is high in a very narrow space near the (negatively) charged pore wall. In the pore center it is low, but significantly above the value at the controlling edges (upper or lower). The $\mathrm{co_{K,o}}$ is similar in value near the pore wall, but is near zero close to the (positively charged) disk. Given that in between the pore and disk walls it differs significantly from the $\mathrm{co_{K,u}}$, there is a significant $\mathrm{co_K}$ axial gradient in small space near the disk tip. The $\mathrm{co_{Cl,u}}$ is low near the pore wall and rises towards its center, whereas the $\mathrm{co_{Cl,o}}$ (also low near the wall) rises to high values near the (positively) charged disk.

Neither the $\mathrm{co_{K,u}}$ (and $\mathrm{co_{K,o}}$) nor $\mathrm{co_{Cl,u}}$ (and $\mathrm{co_{Cl,o}}$) radial profiles change significantly, if the E_ex is reversed (Fig. 2A, B). However, as can be seen from 2D distributions the panels of $\mathrm{c_K}$ (and $\mathrm{c_{Cl}}$) are not identical if V_u is reversed. The $\mathrm{co_{K,u}}$ (and $\mathrm{co_{K,o}}$) and $\mathrm{co_{Cl,u}}$ (and $\mathrm{co_{Cl,o}}$) radial profiles should reveal some differences if different axial positions are chosen. The $E_\mathrm{ax,u}$ and $E_\mathrm{ax,o}$ radial profiles (which are quite uniform) change with the E_ex reversal. The $\mathrm{E_{ax,o}}$ profiles change too but more so (Fig. 2C). Complete $\mathrm{V_u}$ dependence reveals that the $\mathrm{co_K}$ and $\mathrm{co_{Cl}}$ (near the pore wall and in the pore center) are both qualitatively similar–high at very positive and negative V_us, and low at zero V_u (Fig. 2D, E). The $E_\mathrm{ax,u}$s however depend on the V_u linearly, but the $E_\mathrm{ax,o}$s are higher and more $\mathrm{V_u}$-dependent than the $E_\mathrm{ax,u}$s (Fig. 2F).

All axial current densities–migratory ($\sigma_\mathrm{I,mig}$), diffusive ($\sigma_{\text{I'diff}}$) and convective ($\sigma_\mathrm{I,conv}$)–are affected by the $\mathrm{E_{ex}}$ (Fig. 3). Figure 3A-D show their radial profiles and those of the total current density ($\sigma_{\text{I'tot}}$) for two extreme V_us. The $\sigma_\mathrm{I,conv,u}$ is confined largely to the spaces near the pore wall (being zero near pore center)–a consequence of the presence of E_ax and elevated ion (counter-ion) concentration there that drive the water flow. When water flow changes direction with the E_ax reversal the $\sigma_\mathrm{I,conv,u}$ changes direction too. The $\sigma_{\text{I'diff,u}}$ is also prominent near the pore wall and this is due to large $\mathrm{co_K}$ and $\mathrm{co_{Cl}}$ axial gradients there (see the difference of $\mathrm{co_{K,u}}$ and $\mathrm{co_{K,o}}$ (and $\mathrm{co_{Cl,u}}$ and $\mathrm{co_{Cl,o}}$) radial profiles (Fig. 2A, B)). The $\sigma_{\text{I'diff,u}}$ profiles do not change significantly if the E_ex is reversed, and this is not surprising because the $\mathrm{co_K}$ and $\mathrm{co_{Cl}}$ radial profiles do not change either. The $\sigma_\mathrm{I,mig,u}$ (the largest of all) is however non-zero at any radial distance, and its radial profiles are reversed with E_ax reversal. Two factors explain $\sigma_\mathrm{I,mig,u}$ profiles–non-zero and constant E_ax at any

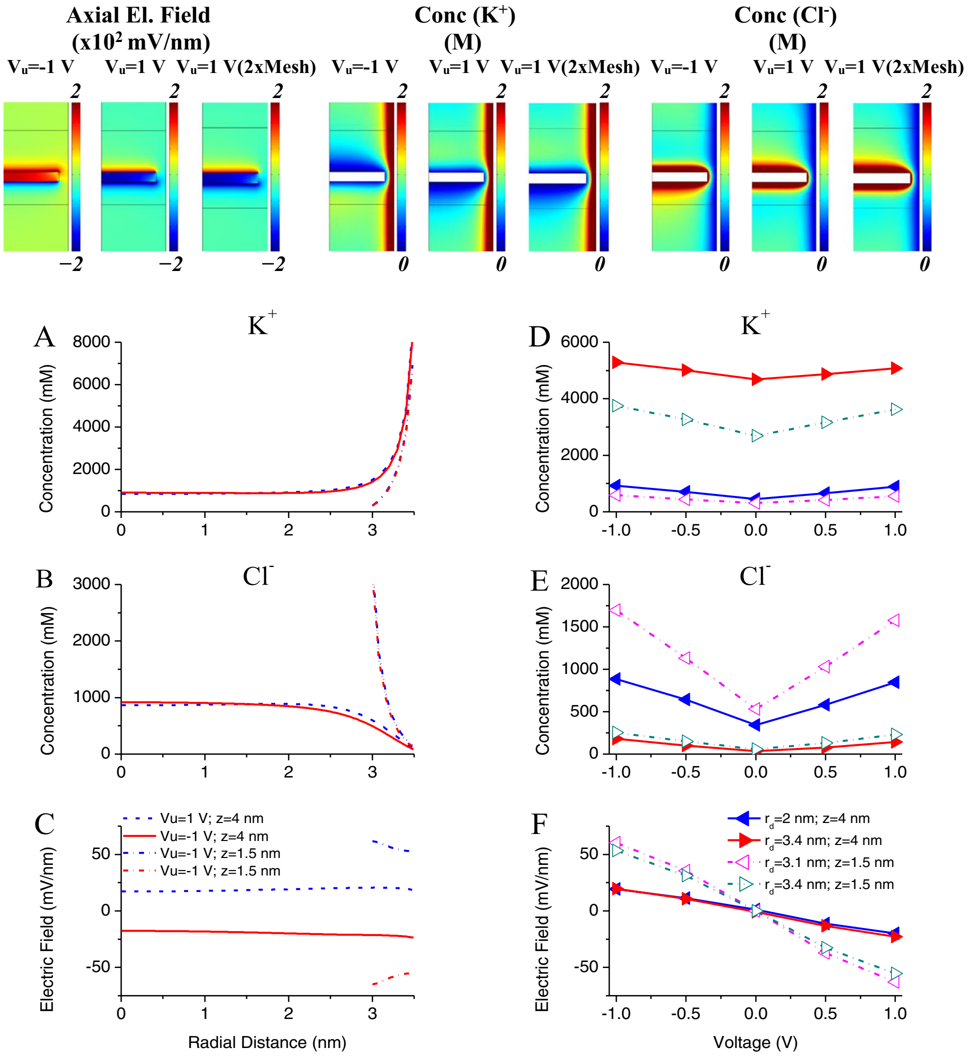

Fig. 2 Effect of external electric field on electric field and ion concentrations within a nanopore. External axial electric field (E_{ex}) alters axial electric field (E_{ax}) within a cylindrical nanopore with charged walls and an object (a disk), but also K^+ and Cl^- concentrations (co_K and co_{Cl}). Disk radius (r_o) was 3 nm, charge density at the pore wall (σ_w) was −160 mC/m^2 (this is equivalent to 1 e/nm^2), and at the disk (σ_o), it was +160 mC/m^2. Ion concentrations (K^+ and Cl^-) at the controlling edges of the upper (co_u) and lower (co_d) compartment were 400 mM. The color coded 2D distributions of E_{ax}, co_K and co_{Cl} are given on top for the voltage at upper controlling edges (V_u) with $V_u = -1$ V (left panels), +1 V (middle panels) and +1 V but with mesh doubled in size (right panels). In this case and throughout the text the potential (V_d) at the lower controlling edges was 0 V, whereas the pressure at both upper and lower controlling edges was 0 Pa (see Table 1). The calibration bars are as indicated. **A**, **B** Radial profiles of K^+ concentrations at $z = 4$ nm (i.e., 2.25 nm above the disk upper surface and from pore center to the wall; $co_{K,u}$), or at $z = 1.5$ nm (i.e., from the axial center of the disk to the pore wall; $co_{K,o}$) and corresponding Cl^- concentrations ($co_{Cl,u}$ and $co_{Cl,o}$). **C** Radial profiles of $E_{ax,u}$ and $E_{ax,o}$. **D**, **E** V_u dependence of $co_{K,u}$ (and $co_{K,o}$) and $co_{Cl,u}$ (and $co_{Cl,o}$) near the pore wall and in the pore center. **F** V_u dependence of $E_{ax,u}$ and $E_{ax,o}$

radial distance, whose values reverse with E_{ax} reversal, and co_K and co_{Cl} radial profiles that are essentially insensitive to the E_{ex} reversal (Fig. 2A, B).

The V_u-dependence plots of the Is summarize these findings. The migratory currents ($I_{mig,u}$ and $I_{mig,o}$), which are the greatest at all V_us, depend linearly on the V_u (Fig. 3E-H). Given that neither the co_Ks nor co_{Cl}s change greatly with the V_u (and thus the $E_{ax,u}$ and $E_{ax,o}$) reversal, and the fact that the E_{ax} changes linearly with the E_{ex}, linear dependence of I_{mig}s is as expected. The K^+ contributes the most to the I_{mig}, and this is also as expected–K^+ is a counter-ion to the negatively charged pore wall. Note that the $I_{conv,u}$ and $I_{conv,o}$ also depend linearly on V_u, unlike the $I_{diff,u}$ and $I_{diff,o}$ that do not. Finally, note that if there is no disk the $I_{conv,u}$ becomes more V_u-dependent whereas the $I_{mig,u}$ and $I_{tot,u}$ become less so. Small and largely V_u-independent $I_{diff,u}$ becomes even smaller and less V_u-dependent.

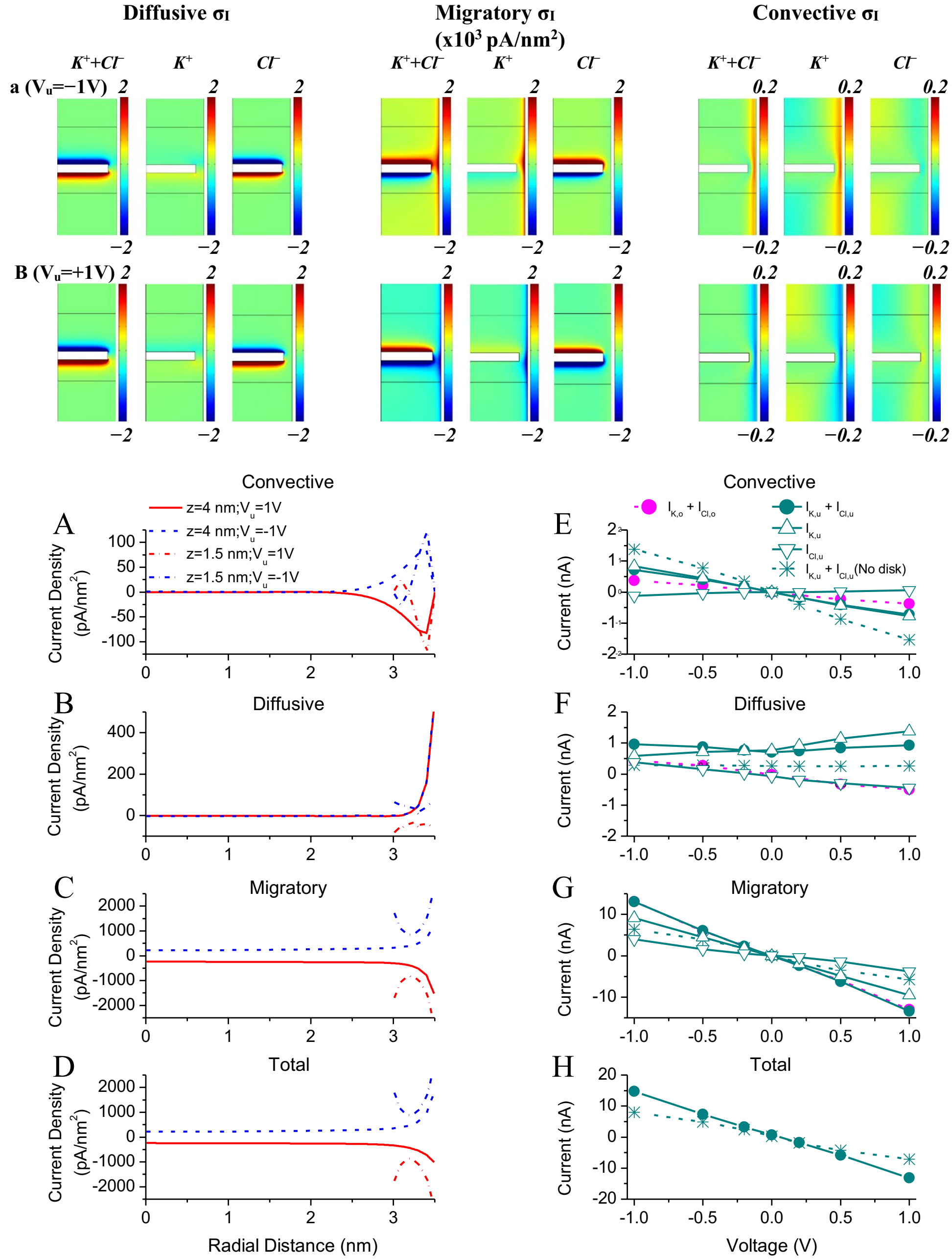

Fig. 3 Effect of external electric field on ion currents. The color-coded 2D distributions of ion current densities (convective–$\sigma_{I,conv}$, diffusive–$\sigma_{I,diff}$, migratory–$\sigma_{I,mig}$, and total–$\sigma_{I,tot}$) are given on top for the $V_u = -1$ V (a; upper panels) or +1 V (b; lower panels; the same simulations as in Fig. 2). The K^+ and Cl^- contributions and their sum are shown separately. The $\sigma_{I,mig}$ is clearly affected and to a lesser extent the $\sigma_{I,conv}$ by V_u change. **A**–**D** Radial profiles of $\sigma_{I,conv,u}$, $\sigma_{I,diff,u}$, $\sigma_{I,mig,u}$, and $\sigma_{I,tot,u}$ and $\sigma_{I,conv,o}$, $\sigma_{I,diff,o}$, $\sigma_{I,mig,o}$, and $\sigma_{I,tot}$ for the V_u as indicated. The $\sigma_{I,mig}$ clearly dominates and largely determines the amplitude and the shape of the $\sigma_{I,tot}$. The V_u-dependence of $I_{conv,u}$ and $I_{conv,o}$ (**E**), $I_{diff,u}$ and $I_{diff,o}$ (**F**), and $I_{mig,u}$ and $I_{mig,o}$ (together with their K^+ and Cl^- contributions; **G**), and I_{tot} (**H**). V_u-dependence of the $I_{conv,u}$, $I_{diff,u}$, $I_{mig,u}$, and $I_{tot,u}$ in the absence of a disk is also given (as indicated)

3.2 Effect of External Ion Concentrations on Currents

If the external K^+ and Cl^- concentrations (they are identical at both sides of the nanopore throughout this study) change, the co_K and co_{Cl} will also change. How large the change is and where, is important as it influences the E_{ax} and ultimately the current–its all three components. In the presence of an object the change may be difficult to predict. DNA translocation reduces the current compared to the baseline current at high concentration, but at low concentration it increases it [45]. As Fig. 4 shows the effect on the co_Ks and co_{Cl}s is qualitatively as expected. The $co_{K,u}$ near (negatively charged) pore wall is high, but changes only moderately. In the pore center it is low but depends more on the external concentrations. Interestingly, it is above the external value (Fig. 4A, D). The $co_{K,o}$ is also low (but not as low as the $co_{K,u}$) near the pore wall (the disk is positively charged), but rises more as external concentrations increase.

The $co_{Cl,u}$ and $co_{Cl,o}$ are also as expected near zero close to the pore wall, especially when the external concentrations are low. In the pore center, the $co_{Cl,u}$ is above the external values (the disk is positively charged) and higher at high external concentrations. Finally, the $co_{Cl,o}$ is quite high near the disk and very dependent on external concentration (Fig. 4B, E). In general thus the co_{Cl}s also rise as the external concentrations increase but those that are the largest (the $\text{co}_{\text{Cl,o}}$ near the disk and the $\text{co}_{\text{Cl,u}}$ near the pore center) rise the most (Fig. 4E). It is intuitively not very obvious how the $E_{\text{ax,u}}$ or $E_{\text{ax,o}}$ radial profiles may be influenced by the external co_{K} and co_{Cl}. As these simulations show they both become more negative at high external K^+ and Cl^- concentration especially in the pore wall-disk space (Fig. 4C, F).

What should σ_{I} profiles be given such co_{K}, co_{Cl}, and E_{ax} radial profiles? The $\sigma_{\text{I,conv,u}}$ which is small and negative near the pore center (but zero at the pore or disk walls; see Sect. 2) has a negative peak near the pore wall. The $\sigma_{\text{I,conv,o}}$ peak is also negative but is larger. They both become more negative at higher external concentrations (Fig. 5A). Elevated K^+ concentration near positively charged pore wall and positive V_{u} lead to negative I_{tot}, that drives negative water flow (not shown) and thus negative I_{conv}, which becomes more negative at high external concentrations, and this remains the case regardless of axial position. The $\sigma_{\text{I,diff,u}}$ is positive and elevated near the pore wall but very insensitive to the external concentration change, whereas the $\sigma_{\text{I,diff,o}}$ is negative and small but depends on external concentration (Fig. 5B). Positive $\sigma_{\text{I,diff,u}}$ is not surprising due to an axial K^+ concentration gradient induced by the positive V_{u}, but it is more difficult to predict what the $\sigma_{\text{I,diff,o}}$ would be because of complex c_{K} and c_{Cl} distributions in disk-pore wall space. Finally, the $\sigma_{\text{I,mig,u}}$ is near zero in the pore center and negative near the pore wall at low concentrations. It becomes negative even in the pore center but especially near the pore wall at high concentrations. This is due to the significantly greater $\text{co}_{\text{Cl,u}}$ throughout nanopore and negative and larger E_{ax} (Fig. 4). The $\sigma_{\text{I,mig,o}}$ is negative in the disk-pore wall space at low or high concentrations. This becomes much more so at elevated external concentrations near both the disk and pore wall. Given that the $\sigma_{\text{I,mig}}$ is the largest it determines the $\sigma_{\text{I,tot}}$ profile (Fig. 5C, D). Finally, note that with no disk the $I_{\text{conv,u}}$ becomes more concentration dependent whereas the $I_{\text{mig,u}}$ and $I_{\text{tot,u}}$ become less so. Small $I_{\text{diff,u}}$ becomes smaller and essentially concentration independent.

How Is depend on external concentrations is sometimes easy to predict, but not always. The total $I_{\text{conv,u}}$ and $I_{\text{conv,o}}$ are small but increasing as the external concentrations rise. They are carried largely by K^+ ions concentrated near the negatively charged pore wall (Fig. 5E). The total $I_{\text{diff,u}}$ is small, positive (carried by K^+ ions and increasing modestly as the external concentration rises). Interestingly, the total $I_{\text{diff,o}}$ which is even smaller is negative and carried by the Cl^- ions (Fig. 5F). The $I_{\text{mig,u}}$ and $I_{\text{mig,o}}$ (the largest at any concentration and which determine the $I_{\text{tot,u}}$ and $I_{\text{tot,o}}$), which are negative and almost identical, increase as external concentrations rise (Fig. 5G, H). Finally, we show the 2D distributions with relative error needed to terminate simulations reduced by ten times (third panel in each case). This did not lead to any visible change demonstrating that the chosen relative error is adequately small.

3.3 Effect of Pore Wall Charges on Ion Currents

How much do the pore wall charges affect co_{K} and co_{Cl} within the nanopore with a charged disk, and what are the consequences for ion currents passing through? If the σ_{w} changes from -160 to 0 mC/m^2 to $+160$ mC/m^2, the co_{K} and co_{Cl} change greatly throughout the nanopore. The changes near the pore wall are as expected. Away from the pore wall, the co_{K} changes little above the disk when σ_{w} changes from -160 to 0 mC/m^2 but increases significantly when the σ_{w} rises to $+160$ mC/m^2. Below the disk the co_{K} decreases to very low levels before rising, but very modestly. Interestingly, the co_{Cl} changes similarly both above and below the disk. The σ_{w} influences the E_{ax} too but the effect is confined to or near the disk (Fig. 6).

The radial profiles confirm visual impressions. Near the pore wall, the $\text{co}_{\text{K,u}}$ and $\text{co}_{\text{K,o}}$ are either high (negative σ_{w}), the same as the $\text{co}_{\text{K,u}}$ in the pore center (zero σ_{w}) or low (positive σ_{w}). In the pore center, the $\text{co}_{\text{K,u}}$ is in all cases above the external value but is especially elevated for positive σ_{w}–probably an effect of positive V_{u} (Fig. 6A). The $\text{co}_{\text{Cl,u}}$ near the pore wall is also easy to predict–high near positive wall, zero if it is negative and the same as in the pore center if the σ_{w} is zero. In the pore center, it is always above its external value, but higher for positive σ_{w}. It is high near the (positively charged) disk but is still influenced by the σ_{w} (Fig. 6B). The effect of σ_{w} on the E_{ax} is interesting. Whereas the $\text{E}_{\text{ax,u}}$ is always negative (with flat radial profile), it is more negative for negative σ_{w}. Finally, the $E_{\text{ax,o}}$ is both much more negative, and much more σ_{w} dependent (Fig. 6C). We also evaluated the E_{rad}. If σ_{w} changes the $E_{\text{rad,u}}$ should also change, and it does from being very near zero at radial distances below 2 nm to very significantly positive beyond (if the σ_{w} is negative) or similarly significantly negative (positive σ_{w}). If σ_{w} is zero, the $E_{\text{rad,u}}$ rises to positive but small values (Fig. 6C$_1$).

The σ_{w} dependence of co_{K}, co_{Cl}, and E_{ax} provides some additional insights. As the σ_{w} changes from negative to positive, the $\text{co}_{\text{K,u}}$ and $\text{co}_{\text{K,o}}$ decrease from very high to low values near the pore wall, whereas in the pore center the $\text{co}_{\text{K,u}}$ rises from low values, and near the disk the $\text{co}_{\text{K,o}}$ remains low (Fig. 6D). In contrast, the $\text{co}_{\text{Cl,o}}$ rises greatly near the disk and pore walls, whereas the $\text{co}_{\text{Cl,u}}$ rises similarly near the pore wall but its rise in the pore center is less pronounced (Fig. 6E). Finally, the $E_{\text{ax,u}}$ is negative and not very σ_{w} dependent, whereas the $E_{\text{ax,o}}$ is much more negative and its σ_{w} dependence is complex (Fig. 6F).

The σ_{w} effect on σ_{I}s is pronounced but some changes are surprising (Fig. 7). The $\sigma_{\text{I,conv,u}}$ (zero in the pore center) is

Fig. 4 Effect of external ion concentrations on concentrations and electric field within nanopore. Color-coded 2D distributions depict the effect of external ion concentrations on the co_K, co_{Cl} and E_{ex} within nanopore. The V_u was 1 V, the σ_w was −160 mC/m^2, and the σ_o was +160 mC/m^2. Radial profiles of $co_{K,u}$ and $co_{K,o}$ (**A**), $co_{Cl,u}$ and $co_{Cl,o}$ (**B**), and E_{ax} (**C**) at external co_K and co_{Cl} as indicated. Concentration dependence of $co_{K,u}$ and $co_{K,o}$ (**D**) $co_{Cl,u}$ and $co_{Cl,o}$ (**E**) and $E_{ax,u}$ and $E_{ax,o}$ (**F**) near the pore wall, and in the pore center (or near the disk wall)

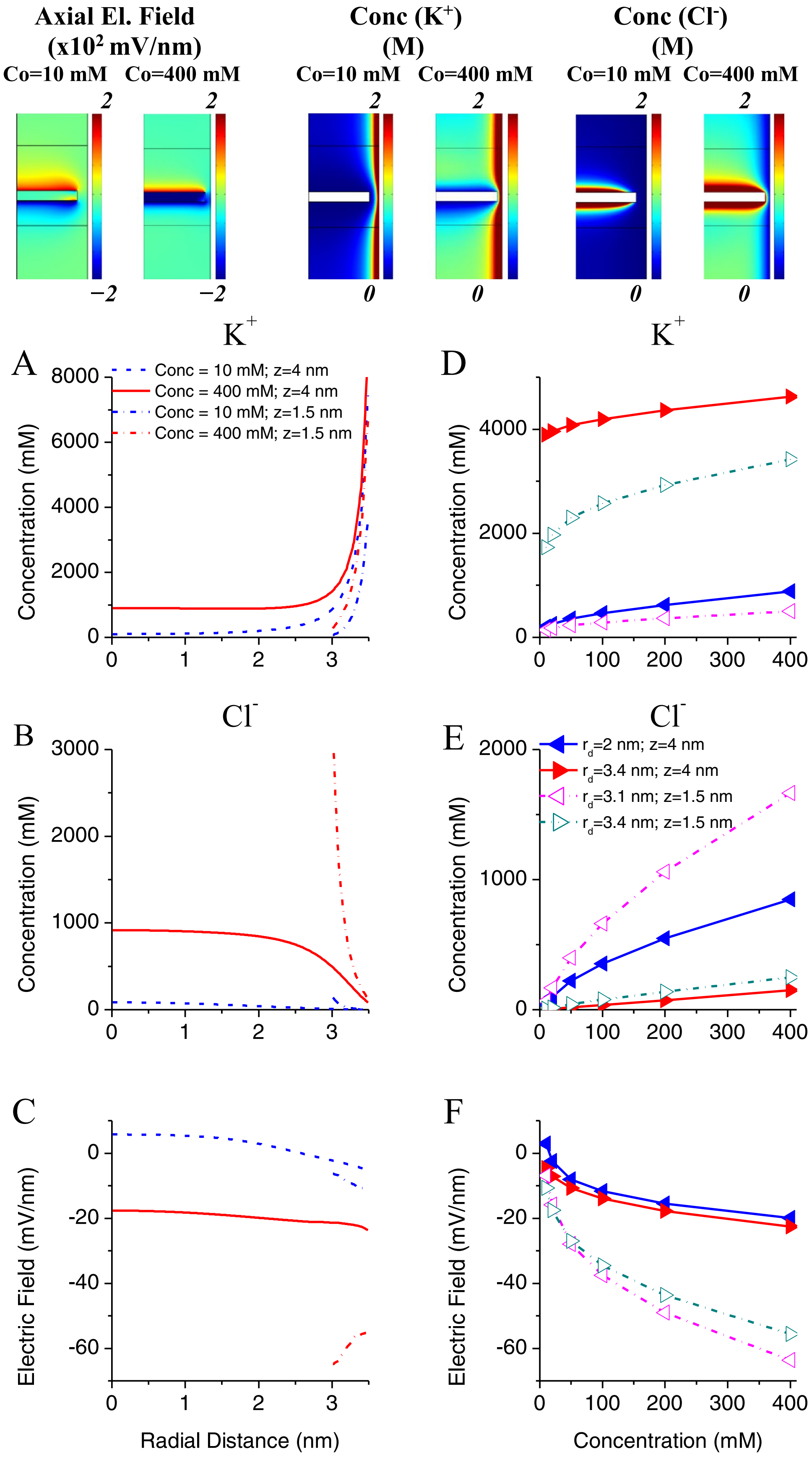

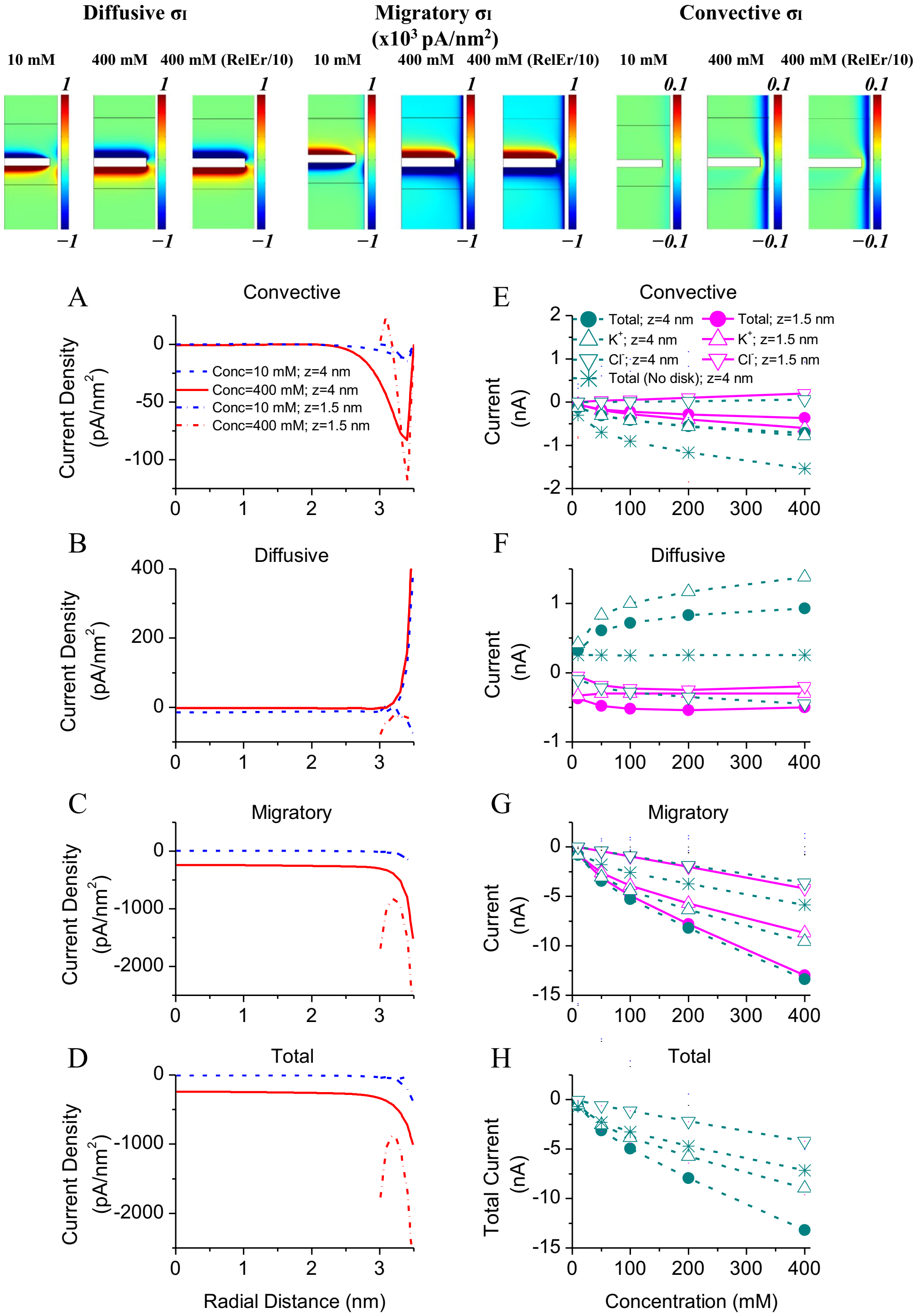

Fig. 5 Effect of external ion concentrations on current densities within nanopore. The $\sigma_{I,conv}$ and $\sigma_{I,mig}$ depend significantly on external ion concentrations, but changing the relative error needed to terminate simulations led to no visible change (see text;. see 2D color-coded distributions on top with external concentrations as indicated). Third panels indicate results with relative error reduced by ten times (the same simulations as in Fig. 4). Radial profiles of $\sigma_{I,conv,u}$, $\sigma_{I,conv,o}$ (**A**), $\sigma_{I,diff,u}$ and $\sigma_{I,diff,o}$ (**B**), $\sigma_{I,mig,u}$ and $\sigma_{I,mig,o}$ (**C**) and $\sigma_{I,tot,u}$ and $\sigma_{I,tot,o}$ (**D**). Concentration dependence of $I_{conv,u}$ and $I_{conv,o}$ (**E**), $I_{diff,u}$ and $I_{diff,o}$ (F) and $I_{mig,u}$ and $I_{mig,o}$ (**G**) and I_{tot} (**H**) with K$^+$ and Cl$^-$ contributions for the selected loci as indicated. Concentration dependence of the $I_{conv,u}$, $I_{diff,u}$, $I_{mig,u}$ and $I_{tot,u}$ with no disk within nanopore is also shown (as indicated)

negative near the pore wall regardless of σ_w sign, but more so if the σ_w is negative. The $\sigma_{I,conv,o}$ is more negative than $\sigma_{I,conv,u}$ for similarly charged pore wall and disk. However, it is positive near the disk and negative near the wall if the σ_o and σ_w differ in sign (Fig. 7A). This is not surprising because water movement drives positive and negative ions in the same direction. What the $\sigma_{I,diff}$ radial profiles should be is intuitively less obvious, owing to the spatial complexity of co_K and co_{Cl} near the disk and pore walls. The $\sigma_{I,diff,u}$ is zero in the pore center, negative near positively charged pore wall, but positive if it is negative. As already discussed this is likely due to the V_u that affects K$^+$ and Cl$^-$ differently. The $\sigma_{I,diff,o}$ is positive near positively charged pore wall, but negative and small if it is negatively charged (in both cases the disk was positively charged; Fig. 7B). The $\sigma_{I,mig,u}$ is negative at any radial distance but more so near the pore wall (especially if the σ_w is negative), as is the $\sigma_{I,mig,o}$ which is larger and negative near both the disk and the pore walls

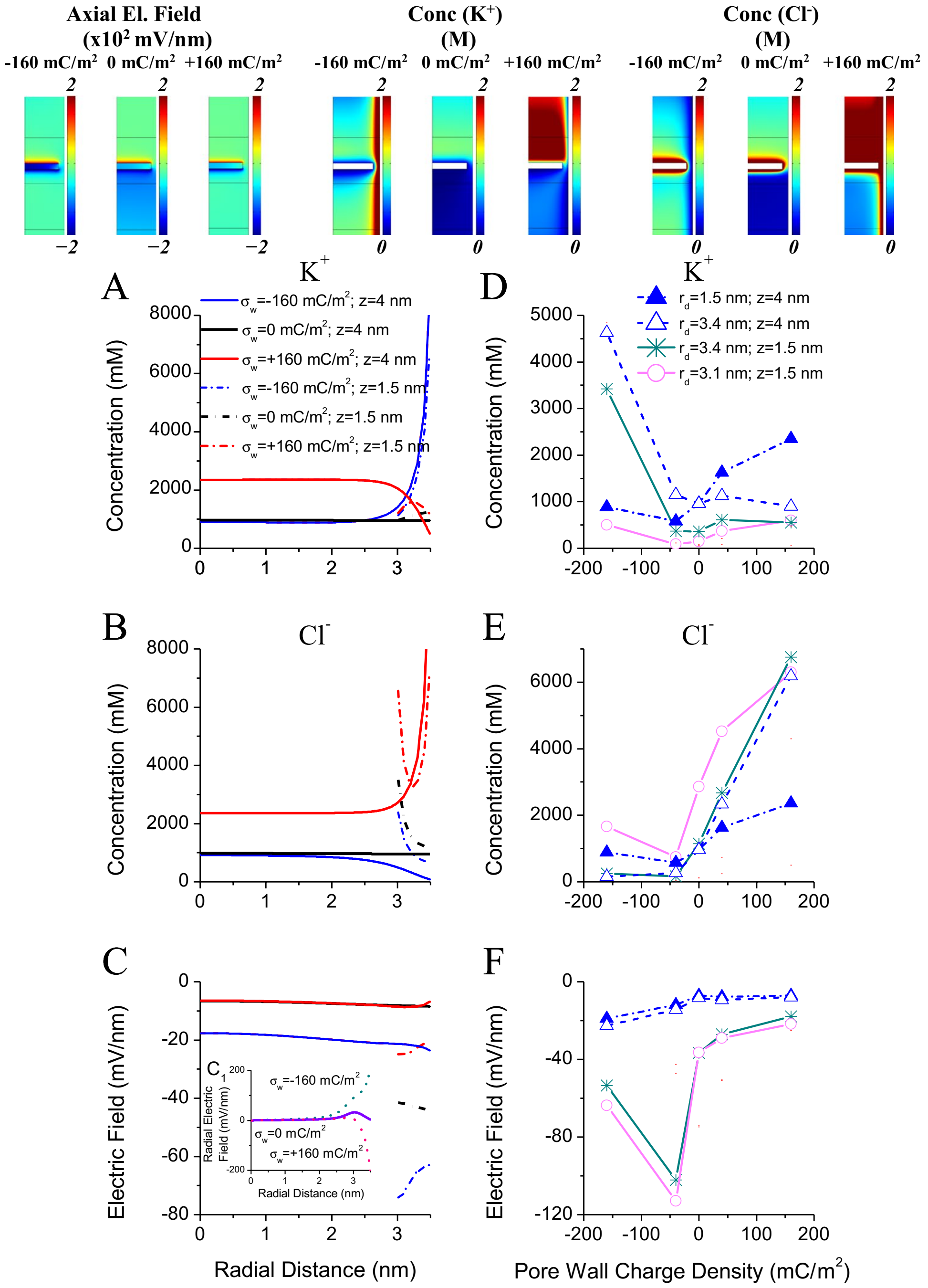

Fig. 6 Effect of pore wall charges on concentrations and electric field within nanopore. The co_K, co_{Cl}, and E_{ax} are all σ_w dependent (see 2D color-coded distributions on top). The V_u was 1 V, the external co_K and co_{Cl} were 400 mM, and the σ_o was +160 mC/m^2. Radial profiles of $co_{K,u}$ and $co_{K,o}$ (**A**), $co_{Cl,u}$ and $co_{Cl,o}$ (**B**). **C** Radial profiles of $E_{ax,u}$ and $E_{ax,o}$. C$_1$ Radial profiles of E_{rad} with the σ_w being −160 mC/m^2, 0 mC/m^2, and +160 mC/m^2. The σ_w dependence of $co_{K,u}$ and $co_{K,o}$ (**D**), $co_{Cl,u}$ and $co_{Cl,o}$ (**E**) and $E_{ax,u}$ and $E_{ax,o}$ at selected loci as indicated

regardless of the sign of their charges (Fig. 7C). Negative $\sigma_{I,mig}$s are not surprising given the positive V_u. As expected the $\sigma_{I,tot}$ is similar to that of $\sigma_{I,mig}$ (the $\sigma_{I,conv}$ and $\sigma_{I,diff}$ are much smaller; Fig. 7D).

The radial current densities ($\sigma_{I,rad}$s) just above the upper disk surface (0.25 nm above) were also estimated. If the radial currents are significant, they may contribute to the axial currents in the disk-pore wall space. The $\sigma_{I,rad,conv}$s are small (not shown). The $\sigma_{I,rad,diff}$s are indeed comparable to $\sigma_{I,diff}$s. If the σ_w is negative, the $\sigma_{I,rad,diff}$ is present even at short radial distances and gradually increases near the disk's tip. If the σ_w is positive, the $\sigma_{I,rad,diff}$ is smaller and negative up to the disk's tip, but then it rises to significant and positive values. Interestingly, if the σ_w is zero, the $\sigma_{I,rad,diff}$ remains significant and negative near the tip (Fig. 7 B1). The $\sigma_{I,rad,mig}$s are also elevated and high near the tip, but they oppose the $\sigma_{I,rad,diff}$s (Fig. 7 C1). Finally, the $\sigma_{I,rad,tot}$s are moderate, present at any radial distance, rise near the tip, and are insensitive of the σ_w sign (Fig. 7 D1).

The $I_{mig,u}$ and $I_{mig,o}$ are the largest of all Is and very similar–negative (especially for high σ_w) and essentially independent of σ_w sign (Fig. 7G). Both the $I_{conv,u}$ and $I_{conv,o}$ are

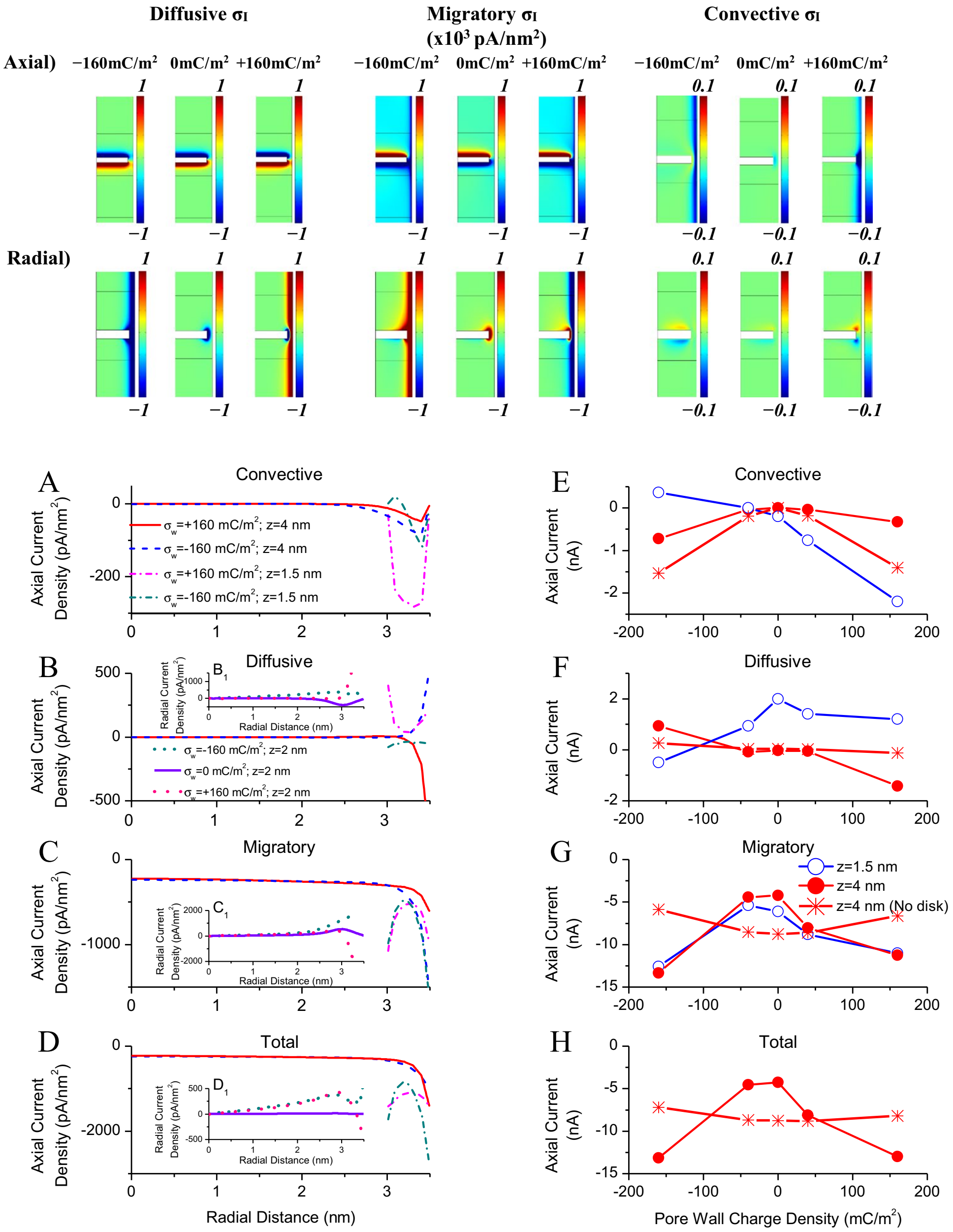

Fig. 7 Effect of pore wall surface charge density (σ_w) on migratory and convective current densities is significant. See 2D color-coded distributions on top (the same simulations as in Fig. 6). Radial profiles of $\sigma_{I,conv,u}$ and $\sigma_{I,conv,o}$ (**A**), $\sigma_{I,diff,u}$ and $\sigma_{I,diff,o}$ (**B**), $\sigma_{I,mig,u}$ and $\sigma_{I,mig,o}$ (**C**), and $\sigma_{I,tot,u}$ and $\sigma_{I,tot,o}$ (**D**). The σ_w and axial distance z were as indicated. Radial profiles of $\sigma_{I,rad,diff}$ (B_1), $\sigma_{I,rad,mig}$ (C_1) and $\sigma_{I,rad,tot}$ (D_1). The σ_w and axial distance z were as indicated. The σ_w-dependence of $I_{conv,u}$ and $I_{conv,o}$ (**E**), $I_{diff,u}$ and $I_{diff,o}$(**F**), $I_{mig,u}$ and $I_{mig,o}$(G), and I_{tot} (**H**) at selected loci as indicated. Dependence of the $I_{conv,u}$, $I_{diff,u}$, $I_{mig,u}$, and $I_{tot,u}$ on σ_w in the absence of a disk is also depicted (as indicated)

small and depend differently on σ_w (Fig. 7E), and the same is true for $I_{diff,u}$ and $I_{diff,o}$ (Fig. 7F). The $I_{tot,u}$ and $I_{tot,o}$ overlap completely (Fig. 7H). If no disk is present within nanopore, the $I_{conv,u}$ becomes more σ_w-dependent. The $I_{mig,u}$ and $I_{tot,u}$ become not only less σ_w-dependent, but also smaller in value at higher σ_w regardless of its sign. Finally, the $I_{diff,u}$ becomes near zero at any σ_w.

3.4 In an Uncharged Nanopore, the Current Magnitude Diminishes as the Disk Size Increases

As already stated, the I_{tot} is the smallest if the σ_w is near zero. Interestingly in such a case, the r_o dependence is qualitatively different. The 2D distributions shown on top compare the σ_Is, E_{ax}, and co_{Cl} for a short and long disk when the σ_w is zero or positive and significant (i.e., 0 or +160 mC/m²; Fig. 8). It is not evident based on visual observations whether or how I_{diff}s will differ, when the σ_w is +160 mC/m² instead of 0 mC/m² regardless of disk radius. Both the I_{conv} and I_{mig} are clearly more negative when the σ_w is +160 mC/m² instead of 0 mC/m² especially near the pore wall. The co_{Cl} and E_{ax} distributions are also shown as they illustrate complex co_{Cl} (especially near the pore wall) and E_{ax} (in the pore interior) changes that influence different currents. The Cl^- is depicted because it is a dominant ion within the nanopore (either both the σ_w

and σ_o are positive or the σ_o is positive and the σ_w is zero; Fig. 8).

Figure 8A and B give the E_{ax} and co$_{Cl}$ axial profiles at the radial mid-point of the disk-pore wall space (i.e., with the r$_d$ of 2 nm or 3.25 nm and from $z = 1.25$ nm to $z = 1.75$ nm). If the disk is small ($r_o = 0.5$ nm) the axial profiles of both E_{ax} and co$_{Cl}$ are constant. Interestingly even in this case their values depend on the σ_w. If the σ_w is 0 mC/m^2, the E$_{ax}$ is clearly more negative and the co$_{Cl}$ is lower. With large disk ($r_o = 3.0$ nm), the E$_{ax}$ is more negative at the lower end especially when the σ_w is 0 mC/m^{2}but is almost zero at the higher end regardless of the σ_w. The co$_{Cl}$ also changes. It is lower when the σ_w is 0 mC/m^2 especially at the lower end. The E$_{ax}$ and co$_{Cl}$ are thus both affected by the σ_w changes even when the disk is small, but if it is large, they also change significantly axially.

The currents depend also on σ_w and at all disk radii, but there are important differences. If the σ_w is zero, the I_{conv} is

Fig. 8 In a nanopore with an uncharged wall greater disk radius (r_o) leads to smaller total ion current. The color-coded 2D distributions of ion current densities (r_o was either 0.5 or 3.0 nm) and Cl$^-$ concentration and E_{ax} (for a disk whose r_o was 3.0 nm) are shown on top. The V_u was +1 V, the σ_o was +160 mC/m^2, the external co$_K$ and co$_{Cl}$ were 400 mM, and the σ_w was as indicated. **A** Axial profiles of E_{ax} at 0.25 nm distance from the pore wall. **B** Corresponding axial profiles of Cl$^-$ concentration. The r$_o$-dependence of I_{conv} (**C**), I_{diff} (**D**), I_{mig} (**E**), and I_{tot} (**F**) for the σ_w as indicated

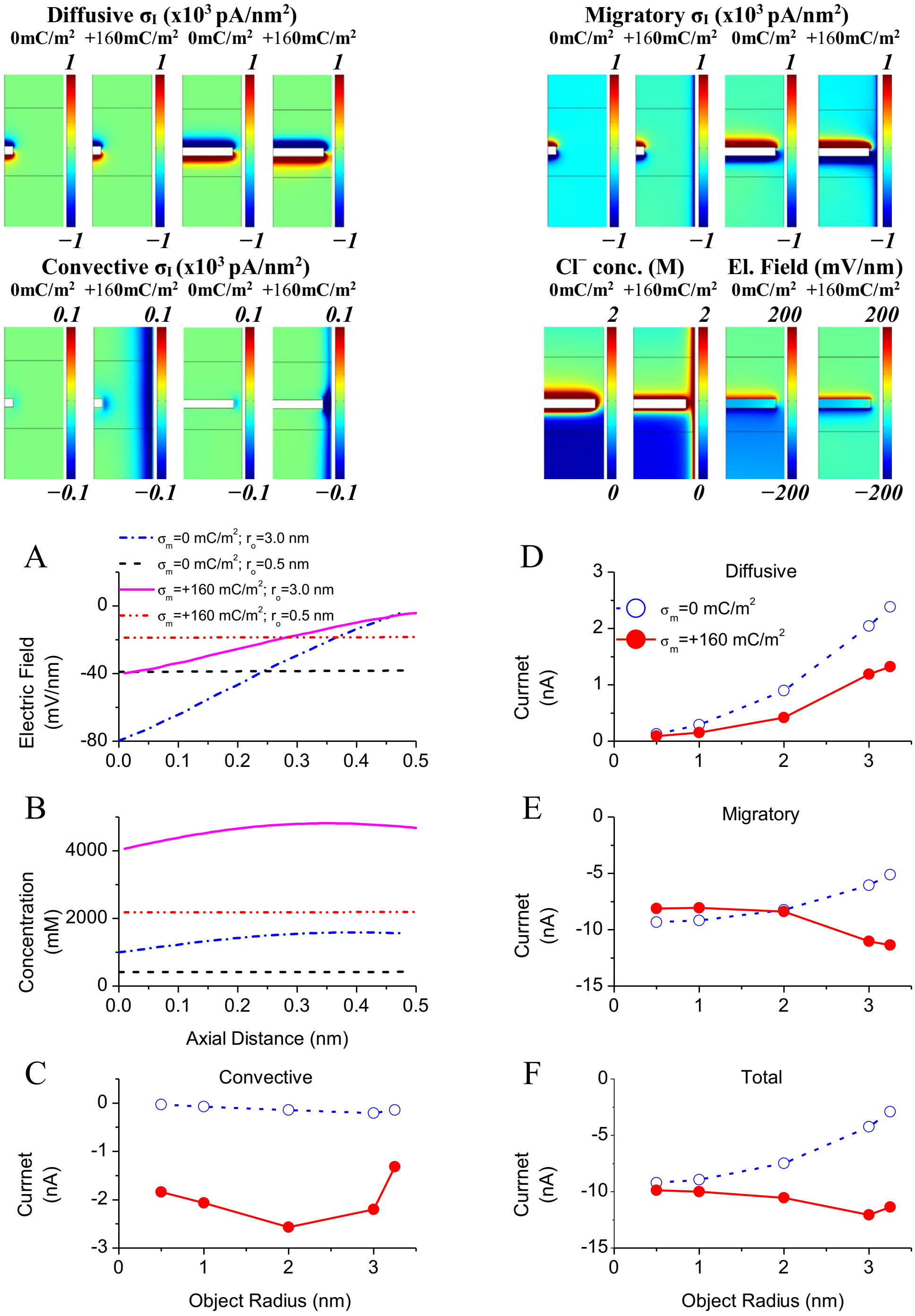

also near zero and is largely r_o-independent. If the σ_w is positive, it is negative (having the most negative value for r_o of 2 nm). There is very little ion accumulation near uncharged pore wall, but if the wall is positively charged Cl^- accumulates. Given that the V_u is positive, water will move upwards (not shown) producing a negative I_{conv}. The I_{conv} decreases eventually when very large disk blocks almost completely mechanically the water flow and I_{conv} (Fig. 8C). The $I_{diff}r_o$-dependence is influenced differently by the σ_w. The I_{diff} is near zero for small r_o regardless of the σ_w. It rises as the r_o increases but more when the σ_w is 0 mC/m^2 (Fig. 8D). Although the co_{Cl} is higher when the σ_w is large and positive, it changes more axially when the σ_w is 0 mC/m^2. When the r_o is small, the co_{Cl} is not only low but changes very little axially (Fig. 8B). The I_{mig} is negative (and the largest of all Is) if the σ_w is 0 mC/m^{2}and diminishes in amplitude (as does the I_{tot}) as r_o increases (Fig. 8E). It is difficult to give a simple explanation for this change–the E_{ax} does not change overall but becomes highly non-uniform axially and the co_{Cl} in fact increases. When the σ_w is positive (+ 160 mC/m^2), the I_{mig} and I_{tot} become more negative with greater r_o (except when the disk comes very near the wall; Fig. 8E, F). The most likely explanation is the rise of Cl^- concentration in the disk-pore wall space (Fig. 8B).

3.5 *At High External Ion Concentrations, Ion Current is More r_o-Dependent*

As external concentrations increase the I_{tot} rises (Fig. 5H), but it is unclear whether, and if so how, its r_o-dependence may change. The V_u remained +1 V but the σ_o(+ 160 mC/m^2) and σ_w(− 160 mC/m^2) differed in sign (unlike in Fig. 8). At two comparatively low but different external concentrations (20 and 100 mM), the I_{conv} diminishes as r_o increases regardless of external concentrations, but its r_o dependence is greater at high concentrations (Fig. 9A). In contrast, the I_{diff} (also small) rises as r_o increases but is concentration independent (Fig. 9B). This is most likely because the axial concentration gradients in the disk-pore wall space–the K^+ (near the pore wall) and Cl^- (near the disk)–increased. Finally, the I_{mig} (the largest current at any r_o; Fig. 9D) is not r_o-dependent at low concentration but at high concentration it is not only larger, but becomes moderately r_o-dependent, rising as r_o increases except when the disk gets very near the pore wall (Fig. 9C).

4 Discussion

4.1 Background

The size of cells and generally micro-particles traversing through a micro-pore is often evaluated by measuring how much their transit reduces the current [2, 46, 47]. A basic idea is that a bigger cell (which leaves smaller cross-sectional area for the passage of ions) leads to smaller current. The cell shape can also be assessed (with irregular micro-pores) from current fluctuations produced by cell rotation [21]. However, it is still not clear why axial irregularity may be critical in inducing object rotation, whether the object would rotate in nanopores, and whether its rotation would be detectable [19–21]. Given that many viruses are at the nanoscale and that thus nanopores will have to be used for their detection a systematic evaluation of what controls the current and current-object size relationship in nanopores is clearly needed.

In this study, we determine using simulations how external factors (electric field and ion concentrations), and pore properties (pore wall charge density) affect the current and object (disk) radius-current relationship in cylindrical nanopores. Three components of axial ionic current are dissected above the disk and in the disk-pore wall space–diffusive (due to concentration gradient; I_{diff}), convective (due to water movement; I_{conv}), and migratory (due to electric field; I_{mig}), as each component is controlled differently. Finally, we dissected the corresponding radial currents and estimate them just above the disk. Note that we do not consider osmotic gradient term in the interaction between ions and the fluid. This will be a part of our future study.

4.2 Effect of External Electric Field on the Current Flow

The effect of external electric field (E_{ex}) on ion currents was tested in a negatively charged nanopore with a positively charged large disk. The voltages applied at the controlling edges resemble those considered previously (ranging from −1 to +1 V; [48]). Greater E_{ex} leads to a proportionally greater I_{mig}, but much smaller I_{conv} and I_{diff} also depend on the E_{ex}. Note that not only at high voltages, but over a wide range of voltages (and thus over a wide range of E_{ex} values), the I_{mig} is the largest current and determines the I_{tot}. At any point within the nanopore, the I_{mig} is determined by two factors: (a) E_{ax} and (b) ion concentrations. We tested the E_{ex} effect above the disk and in the disk-pore wall space. The E_{ax} radial profiles are uniform. The E_{ax} depends (linearly) on the E_{ex}, but its dependence is greater in the pore wall-disk space. As in conically shaped nanopores, the E_{ex} influences the co_K and co_{Cl} [25, 49, 50], which rise with greater E_{ex} regardless of tested location, and independently of E_{ex} polarity. Finally note that the disk presence within nanopore leads to greater V_u-dependence of the $I_{tot,u}$ (and $I_{mig,u}$), but that of the $I_{conv,u}$ diminishes.

4.3 *Effect of External Ion Concentrations on Ion Currents and Their r_o Dependence*

External K^+ and Cl^- concentrations influence those within nanopore, but unequally. The concentrations varied over a

Fig. 9 Ion current is more r_o-dependent at high ion concentrations. The color-coded 2D distributions of ion current densities (the disk whose radius r_o was either 0.5 nm or 3.0 nm) are shown on top. **A**–**D** The r_o dependence of I_{conv}, I_{diff}, I_{mig}, and I_{tot} for $co_{K,u}$ and $co_{Cl,u}$ of 20 mM or 100 mM. The V_u was +1 V, σ_o was +160 mC/m^2 and σ_w was −160 mC/m^2

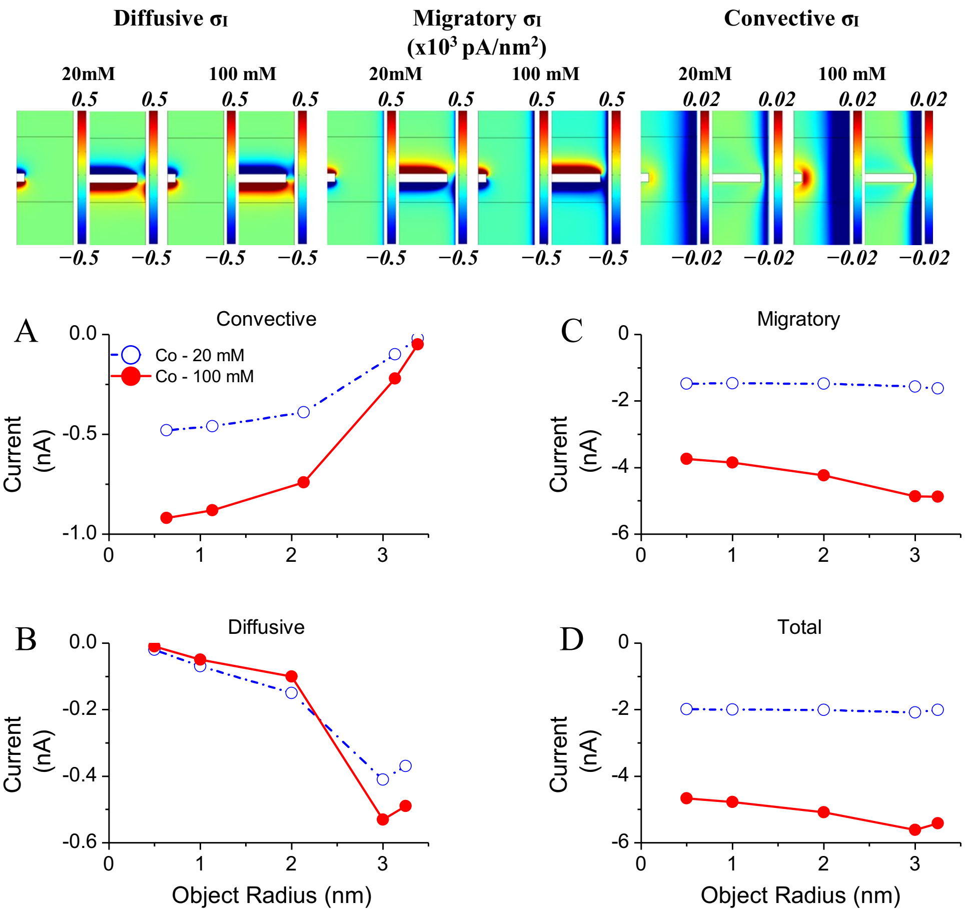

significant range (from 10 to 400 mM)–i.e., beyond values used experimentally (100–300 mM; [20]), and if they rise, the nanopore concentrations increase. Given that in these simulations the pore wall is negatively charged, and disk is positively charged K$^+$ ions are counter-ions for the pore wall and co-ions for the disk surface. Opposite is the case for Cl$^-$ ions. As expected near the pore wall, the co_K is high (but more so above the disk than in the disk-pore wall space), whereas in the pore center it is low but even lower near the disk in the disk-pore wall space. The co_{Cl} is opposite–low near the pore wall above the disk and in the disk-pore wall space. In the pore center, it is high (moderately) but higher near the disk in the disk-pore wall space. As the external concentrations rise, both co_K and co_{Cl} rise regardless of location tested. The co_K increases little near the pore wall above the disk, but more so in the disk-pore wall space. The co_{Cl} remains low near the pore wall, but in the pore center and especially near the disk in the disk-pore wall space, it rises significantly.

The E_{ax} was negative (V_u was +1 V and V_d 0 V) except at low external concentrations in the center of the nanopore. It becomes progressively more negative as external concentrations increased, especially in the pore wall-disk space (near the pore wall or the disk). This is not entirely surprising because in that space the ion concentrations change greatly both radially and axially, especially when the disk almost reaches the pore wall. All current components increase–the I_{mig} (the greatest), the I_{conv} (that adds to the I_{mig}), and the I_{diff} (that opposes it) owing to elevate charges near the pore wall and greater E_{ax}. The I_{tot}, which is r_o independent at low concentration, becomes r_o dependent at high concentration, but only modestly. It is also worth pointing that if the disk is present within the nanopore the concentration dependence of the $I_{tot,u}$ and $I_{mig,u}$ rises but that of the $I_{conv,u}$ diminishes.

4.4 *Effect of Pore Wall Charges on Ion Concentrations and Currents and Current r_o Dependence*

In this study, the σ_w changed from −160 to +160 mC/m^2. These values are equivalent to 1 e/nm^2–thus equal or beyond those observed biologically or used experimentally. At the surface of biological membranes, the σ_w has been estimated at 40–160 mC/m^2 or 0.25 to 1 e/nm^2 [51, 52], and at the surface layer of SiO$_2$ membrane at 26 mC/m^2 [53]. As expected the σ_w influences the ion concentrations greatly near the charged pore wall or disk surfaces. We find it surprising how large the σ_w influence is throughout the nanopore including in the pore center. It is also notable how different the counter-ion and co-ion concentrations could be above and below the disk. The effect on the E_{ax} is also difficult to predict–pronounced and complex in the disk-pore wall space, but also present though limited above the disk.

How σ_I radial profiles and corresponding currents should depend on the σ_w is sometimes possible to assess but not always. As expected the $\sigma_{I,diff}$ and $\sigma_{I,conv}$ are confined near the pore wall regardless of the σ_w value or its sign. However, the $\sigma_{I,mig}$, though greater near the pore wall, is not insignificant near the pore center. The $\sigma_{I,mig}$ rises greatly as σ_w increases but its direction is independent of the σ_w sign. The I_{mig}-σ_w relationship is thus almost parabolic. Greater concentration of counter-ions near the pore wall contributes to greater I_{mig} at higher σ_w. It however does not affect its direction (K^+ movement in one direction is the same as Cl^- movement in the opposite direction). The E_{ax} also changes (especially in the pore wall-disk space) influencing the I_{mig}, but the E_{ax}-σ_w relationship is complex.

Given that the nanopore does not have current sources or sinks, the I_{tot} has to be independent of where axially it is estimated and it is. The I_{mig} which clearly makes the largest contribution to the I_{tot} should thus depend very little on where they are axially estimated, and that is also the case. On the other hand much smaller I_{diff} and I_{conv} may differ significantly depending on where axially they are estimated, and they clearly do. It has been suggested that the (a) presence of an object within nanopore leads to volume exclusion of electrolyte solution thus reducing the axial current flow and (b) charged object induces screening charges leading to larger axial currents, finally producing multi-level current changes [26]. However, this study clearly demonstrates that the $I_{tot,u}$ (and $I_{mig,u}$) become larger and not smaller (regardless of σ_w sign) at high σ_w if disk is present within the nanopore. However, if the σ_w is low (or zero), the $I_{tot,u}$ (and $I_{mig,u}$) become smaller.

To show how the σ_w influences the I-r_o relationship we chose two σ_ws (0 and +160 mC/m^2). In an uncharged nanopore, the I_{mig} decreases in value (rather than increasing) with greater r_o but remains the largest current contribution. The I_{conv} (negative and small for positive σ_w) becomes almost zero for all r_os. The I_{diff} is positive and near zero for small r_o regardless of σ_w. It rises in value with greater r_o but more so in an uncharged nanopore. Should the I_{diff} be positive or negative and how should it change in value as the r_o rises? Consider the Cl^- (counter-ion) concentration near the disk in an uncharged pore. It is elevated near the disk but diminishes upwards. It thus produces a positive I_{diff}. Greater I_{diff} at larger r_o is also not unexpected. Larger r_o leads to more fixed (and thus also more mobile) charges. Whereas a positively charged pore would lead to more charges (Cl^- ions) the axial gradient is likely smaller. Overall, in an uncharged nanopore, the I_{tot} decreases significantly in value with greater r_o, instead of increasing modestly as observed when σ_w is positive and high. A comparison of I-r_o relationships with σ_ws that are either negative or positive but high (the σ_o was +160 mC/m^2 in both cases) is also interesting. The I_{tot}-r_o relationship depends on the σ_w value but is largely independent of its sign (i.e., whether the σ_w and σ_o have the same or opposite signs). However, if the σ_w and σ_o have the same sign, larger I_{tot} at greater r_o is due to higher counter-ion accumulation in the object-pore wall space as suggested before [26]. In contrast, if the σ_w and σ_o are of opposite sign, similarly greater I_{tot} is largely due to an elevated E_{ax} in that space.

It is clear from the above that the uncharged nanopores would make better sensors of size and shape of nano-size objects (such as viruses). Note also, that in a charged nanopore (and to a lesser extent in an uncharged nanopore too), the I_{tot} is almost r_o-independent for r_os ranging from 0 to 2–2.5 nm in a 3.5 nm radius nanopore. Suggestions that the I_{tot} block is due to the volume exclusion of electrolyte solution by the object thus cannot be universally accepted. If the object does not get very close (< 1 nm) to the pore wall, it will not reduce the I_{tot} significantly, because the ion current flows largely in 1 nm space near the pore wall.

Our simulations are three-dimensional based on axial symmetry. True three-dimensional simulations can evaluate radially asymmetrical situations whereby one side of the disk is closer to the pore wall than the opposite side. Given that the I_{tot} depends relatively little on the r_o the I_{tot} should not depend greatly on how asymmetrical the radial position of the disk is. The cross-sectional area for the current flow remains constant. However, if the disk is positioned non-centrally (i.e., if it is axially asymmetrical), the I_{tot} changes. It diminishes linearly if the disk is positioned more upwardly (15 nm change in axial position leads to I_{tot} reduction of 39%; not shown).

4.5 Comment on Continuum Poisson-Nernst-Planck and Navier–Stokes Simulations

Continuum PNP-NS simulations do not capture all features of the nanopore ion and water system. As shown by the molecular dynamics simulations water density and viscosity are greater near the pore wall due to non-electrostatic (described by Lennard–Jones potentials) and electrostatic interactions [54], whereas the Navier–Stokes equations assume that the water is incompressible. The ions are also layered near the pore wall and show a peak near, but not at its surface, because the ions cannot get closer to the surface than an ionic radius [54]. This is also not predicted by the continuum simulations. Nevertheless, most properties of the nanopore ion and water system are well described by the continuum PNP-NS equations for water and ion transport [55].

5 Conclusions

In a charged cylindrical nanopore with a charged disk elevated E_{ex} leads to higher E_{ax}, co_K, co_{Cl}, and I_{tot} (which is largely determined by the I_{mig} regardless of the E_{ex} value). The co_K and co_{Cl} rise (estimated above the disk or in the disk-pore wall space) is largely E_{ex} polarity independent. The I_{tot} also rises with greater σ_w and interestingly it is σ_w sign independent. If the σ_w and σ_o have the same sign, larger I_{tot} is due to higher counter-ion accumulation in the object-pore wall space, but if their signs are opposite similarly larger I_{tot} is mainly due to greater E_{ax} in the object-pore wall space. Elevated external ion concentrations lead to greater co_K and co_{Cl} (mainly away from the pore wall), raise the E_{ax} (especially in the disk-pore wall space), and lead to larger I_{tot}. The I_{tot} is not r_o-dependent at low concentrations, but at high concentrations it is, though only modestly. Surprisingly, at high concentrations the I_{tot} rises modestly when disk becomes bigger. Regardless of external concentrations the I_{tot} depends very little on the r_o if it is < 2 nm. The r_o-independence of I_{tot} for small disks is not surprising because the current flow is largely confined to the space near the pore wall. Smaller cross-sectional area for current flow (size-exclusion principle) or volume exclusion of electrolyte solution by the object thus cannot be universally accepted as explanations of current blockage. However, the radial currents near the charged disk surface due to screening charges and E_{rad} can contribute to axial currents. Finally, if the pore wall is uncharged, the I_{tot} diminishes significantly as r_o increases due to progressively smaller I_{mig}, and larger I_{diff}, which opposes it. Though smaller than the I_{mig}, the I_{diff} is not insignificant.

Author Contribution MIG: conceptualization, simulations, analysis, and writing. MT: model development and writing.

Funding This work was supported by the grant from the Natural Sciences and Engineering Research Council of Canada to M.I.G (Grant no. 24776).

Declarations

Ethics Approval Not applicable.

Competing Interests The authors declare no competing interests.

References

1. Hurley, J. (1970). Sizing particles with a coulter counter. *Biophysical Journal, 10*(1), 74–79. https://doi.org/10.1016/S0006-3495(70)86286-5
2. DeBlois, R. W., & Bean, C. P. (1970). Counting and sizing of submicron particles by the resistive pulse technique. *Review of Scientific Instruments, 41*(7), 909–916. https://doi.org/10.1063/1.1684724
3. Kaiser. G. (2021). *Microbiology*. Community College of Baltimore County, Cantonsville: LibreTexts.
4. Champion, J. A., Katare, Y. K., & Mitragotri, S. (2007). Particle shape: A new design parameter for micro- and nanoscale drug delivery carriers. *Journal of Controlled Release, 121*(1), 3–9. https://doi.org/10.1016/j.jconrel.2007.03.022
5. Mays, T. (2007). A new classification of pore sizes. *Studies in Surface Science and Catalysis, 160*, 57–62.
6. Butler, T. Z., Pavlenok, M., Derrington, I. M., Niederweis, M., & Gundlach, J. H. (2008). Single-molecule DNA detection with an engineered MspA protein nanopore. *Proceedings of the National Academy of Sciences, 2008*, pnas.0807514106. https://doi.org/10.1073/pnas.0807514106
7. Kasianowicz, J. J., Brandin, E., Branton, D., & Deamer, D. W. (1996). Characterization of individual polynucleotide molecules using a membrane channel. *Proceedings of the National Academy of Sciences, 93*(24), 13770–13773. https://doi.org/10.1073/pnas.93.24.13770
8. Moon, J., Kim, N., Kim, T.-J., Jun, J.-S., Lee, H. S., Shin, H.-R., et al. (2019). Rapid diagnosis of bacterial meningitis by nanopore 16S amplicon sequencing: A pilot study. *International Journal of Medical Microbiology, 309*(6), 151338. https://doi.org/10.1016/j.ijmm.2019.151338
9. Nomidis, S. K., Hooyberghs, J., Maglia, G., & Carlon, E. (2018). DNA capture into the ClyA nanopore: Diffusion-limited versus reaction-limited processes. *Journal of Physics: Condensed Matter, 30*(30), 304001. https://doi.org/10.1088/1361-648x/aacc01
10. Ohayon, S., Girsault, A., Nasser, M., Shen-Orr, S., & Meller, A. (2019). Simulation of single-protein nanopore sensing shows feasibility for whole-proteome identification. *PLOS Computational Biology, 15*(5), e1007067. https://doi.org/10.1371/journal.pcbi.1007067
11. Si, W., & Aksimentiev, A. (2017). Nanopore sensing of protein folding. *ACS Nano, 11*(7), 7091–7100. https://doi.org/10.1021/acsnano.7b02718
12. Thakur, A. K., & Movileanu, L. (2019). Real-time measurement of protein–protein interactions at single-molecule resolution using a biological nanopore. *Nature Biotechnology, 37*(1), 96–101. https://doi.org/10.1038/nbt.4316
13. Huang, G., Willems, K., Soskine, M., Wloka, C., & Maglia, G. (2017). Electro-osmotic capture and ionic discrimination of peptide and protein biomarkers with FraC nanopores. *Nature Communications, 8*(1), 935. https://doi.org/10.1038/s41467-017-01006-4
14. Larimi, M. G., Mayse, L. A., & Movileanu, L. (2019). Interactions of a polypeptide with a protein nanopore under crowding conditions. *ACS Nano, 13*(4), 4469–4477. https://doi.org/10.1021/acsnano.9b00008
15. Boersma, A. J., & Bayley, H. (2012). Continuous stochastic detection of amino acid enantiomers with a protein nanopore. *Angewandte Chemie International Edition, 51*(38), 9606–9609. https://doi.org/10.1002/anie.201205687
16. Guo, Y., Niu, A., Jian, F., Wang, Y., Yao, F., Wei, Y., et al. (2017). Metal–organic complex-functionalized protein nanopore sensor for aromatic amino acids chiral recognition. *The Analyst, 142*(7), 1048–1053. https://doi.org/10.1039/C7AN00097A
17. Miyagawa, T., Hongo, S., Nakamura, N., Horiguchi, Y., Miyahara, Y., & Shibata, H. (2018). A novel diagnostic system for infectious diseases using solid-state nanopore devices. In *2018 40th Annual International Conference of the IEEE Engineering in Medicine and Biology Society (EMBC)* (pp. 2833–2836).
18. DeBlois, R. W., Uzgiris, E. E., Cluxton, D. H., & Mazzone, H. M. (1978). Comparative measurements of size and polydispersity of

several insect viruses. *Analytical Biochemistry, 90*(1), 273–288. https://doi.org/10.1016/0003-2697(78)90032-5

19. Yusko, E. C., Bruhn, B. R., Eggenberger, O. M., Houghtaling, J., Rollings, R. C., Walsh, N. C., et al. (2017). Real-time shape approximation and fingerprinting of single proteins using a nanopore. *Nature Nanotechnology, 12*(4), 360–367. https://doi.org/10.1038/nnano.2016.267
20. Qiu, Y., Hinkle, P., Yang, C., Bakker, H. E., Schiel, M., Wang, H., et al. (2015). Pores with longitudinal irregularities distinguish objects by shape. *ACS Nano, 9*(4), 4390–4397. https://doi.org/10.1021/acsnano.5b00877
21. Golibersuch, D. C. (1973). Observation of aspherical particle rotation in Poiseuille flow via the resistance pulse technique. I. Application to human erythrocytes. *Biophysical Journal*, *13*(3), 265–280. https://doi.org/10.1016/s0006-3495(73)85984-3
22. McMullen, A., de Haan, H. W., Tang, J. X., & Stein, D. (2014). Stiff filamentous virus translocations through solid-state nanopores. *Nature Communications, 5*(4171), 1–10. https://doi.org/10.1038/ncomms5171
23. Zhou, K., Li, L., Tan, Z., Zlotnick, A., & Jacobson, S. C. (2011). Characterization of hepatitis B virus capsids by resistive-pulse sensing. *Journal of the American Chemical Society, 133*(6), 1618–1621. https://doi.org/10.1021/ja108228x
24. Acheson, N. H. (2011). *Fundamentals of molecular virology* (2nd ed.). John Wiley & Sons.
25. Lan, W.-J., Kubeil, C., Xiong, J.-W., Bund, A., & White, H. S. (2014). Effect of surface charge on the resistive pulse waveshape during particle translocation through glass nanopores. *The Journal of Physical Chemistry C, 118*(5), 2726–2734. https://doi.org/10.1021/jp412148s
26. Chen, K., Bell, N. A. W., Kong, J., Tian, Y., & Keyser, U. F. (2017). Direction- and salt-dependent ionic current signatures for DNA sensing with asymmetric nanopores. *Biophysical Journal, 112*(4), 674–682. https://doi.org/10.1016/j.bpj.2016.12.033
27. Siwy, Z. S. (2006). Ion-current rectification in nanopores and nanotubes with broken symmetry. *Advanced Functional Materials, 16*(6), 735–746. https://doi.org/10.1002/adfm.200500471
28. Stein, D., Kruithof, M., & Dekker, C. (2004). Surface-charge-governed ion transport in nanofluidic channels. *Physical Review Letters*, *93*(3). https://doi.org/10.1103/PhysRevLett.93.035901
29. Vidal, J., Gracheva, M. E., & Leburton, J.-P. (2007). Electrically tunable solid-state silicon nanopore ion filter. *Nanoscale Research Letters, 2*(2), 61–68. https://doi.org/10.1007/s11671-006-9031-7
30. Perry, R. H., & Green, D. W. (1999). *Perry's Chemical Engineers' Handbook* (7th ed.). *McGraw-Hill*.
31. Tajparast, M., Virdi, G., & Glavinović, M. I. (2015). Spatial profiles of potential, ion concentration and flux in short unipolar and bipolar nanopores. *Biochimica et Biophysica Acta (BBA) – Biomembranes*, *1848*(10, Part A), 2138–2153. https://doi.org/10.1016/j.bbamem.2015.05.023
32. Tajparast, M., Mohammadi, H., & Glavinović, M. I. (2017). Spatial distribution of conductivity in a short charged nanofluidic pore. *Microfluidics and Nanofluidics, 21*(3), 49. https://doi.org/10.1007/s10404-017-1884-9
33. Arima, A., Tsutsui, M., Harlisa, I. H., Yoshida, T., Tanaka, M., Yokota, K., et al. (2018). Selective detections of single-viruses using solid-state nanopores. *Scientific Reports, 8*(1), 16305. https://doi.org/10.1038/s41598-018-34665-4
34. Kovarik, M. L., Zhou, K., & Jacobson, S. C. (2009). Effect of conical nanopore diameter on ion current rectification. *The Journal of Physical Chemistry B, 113*(49), 15960–15966. https://doi.org/10.1021/jp9076189
35. Yang, L., & Yamamoto, T. (2016). Quantification of virus particles using nanopore-based resistive-pulse sensing techniques. *Frontiers in microbiology*, *7*, 1500. https://doi.org/10.3389/fmicb.2016.01500
36. Ali, M., Mafe, S., Ramirez, P., Neumann, R., & Ensinger, W. (2009). Logic gates using nanofluidic diodes based on conical nanopores functionalized with polyprotic acid chains. *Langmuir, 25*(20), 11993–11997. https://doi.org/10.1021/la902792f
37. Gijs, M. A. M. (2007). Will fluidic electronics take off? *Nature Nanotechnology, 2*, 268–270. https://doi.org/10.1038/nnano.2007.116
38. Han, J. H., Kim, K. B., Kim, H. C., & Chung, T. D. (2009). Ionic circuits based on polyelectrolyte diodes on a microchip. *Angewandte Chemie (International ed in English), 48*(21), 3830–3833. https://doi.org/10.1002/anie.200900045
39. Tybrandt, K., Larsson, K. C., Richter-Dahlfors, A., & Berggren, M. (2010). Ion bipolar junction transistors. *Proceedings of the National Academy of Sciences, 107*(22), 9929–9932. https://doi.org/10.1073/pnas.0913911107
40. Bockris, J. O. M., & Reddy, A. K. N. (1976). *Modern electrochemistry*. Plenum Publishing Corporation.
41. Temam, R. (2001). *Navier–Stokes equations, theory and numerical analysis*. AMS Chelsea Publishing.
42. Karniadakis, G. E., Beskok, A., & Aluru, N. (2005). *Microflows and nanoflows: Fundamentals and simulation*. Springer-Verlag.
43. Craven, T. J., Rees, J. M., & Zimmerman, W. B. (2008). On slip velocity boundary conditions for electroosmotic flow near sharp corners. *Physics of Fluids*, *20*(4). https://doi.org/10.1063/1.2906344
44. Savtchenko, L. P., Poo, M. M., & Rusakov, D. A. (2017). Electrodiffusion phenomena in neuroscience: A neglected companion. *Nature Reviews Neuroscience, 18*(10), 598–612. https://doi.org/10.1038/nrn.2017.101
45. Chang, H., Kosari, F., Andreadakis, G., Alam, M. A., Vasmatzis, G., & Bashir, R. (2004). DNA-mediated fluctuations in ionic current through silicon oxide nanopore channels. *Nano Letters, 4*(8), 1551–1556. https://doi.org/10.1021/nl049267c
46. Holden, D., Hendrickson, G., Lan, W.-J., Lyon, L., & White, H. (2011). Electrical signature of the deformation and dehydration of microgels during translocation through nanopores. *Soft Matter, 7*, 8035–8040. https://doi.org/10.1039/C1SM05680H
47. Luo, L., German, S. R., Lan, W.-J., Holden, D. A., Mega, T. L., & White, H. S. (2014). Resistive-pulse analysis of nanoparticles. *Annual Review of Analytical Chemistry, 7*(1), 513–535. https://doi.org/10.1146/annurev-anchem-071213-020107
48. Jou, I. A., Melnikov, D. V., Nadtochiy, A., & Gracheva, M. E. (2014). Charged particle separation by an electrically tunable nanoporous membrane. *Nanotechnology, 25*(14), 145201. https://doi.org/10.1088/0957-4484/25/14/145201
49. Lin, C.-Y., Combs, C., Su, Y.-S., Yeh, L.-H., & Siwy, Z. S. (2019). Rectification of concentration polarization in mesopores leads to high conductance ionic diodes and high performance osmotic power. *Journal of the American Chemical Society, 141*(8), 3691–3698. https://doi.org/10.1021/jacs.8b13497
50. Lin, C.-Y., Yeh, L.-H., & Siwy, Z. S. (2018). Voltage-induced modulation of ionic concentrations and ion current rectification in mesopores with highly charged pore walls. *The Journal of Physical Chemistry Letters, 9*(2), 393–398. https://doi.org/10.1021/acs.jpclett.7b03099

51. Hille, B., Woodhull, A. M., & Shapiro, B. I. (1975). Negative surface charge near sodium channels of nerve: Divalent ions, monovalent ions, and pH. *Philosophical Transactions of the Royal Society of London Series B, Biological sciences, 270*(908), 301–318. https://doi.org/10.1098/rstb.1975.0011
52. McLaughlin, S. G., Szabo, G., & Eisenman, G. (1971). Divalent ions and the surface potential of charged phospholipid membranes. *Journal of General Physiology, 58*(6), 667–687. https://doi.org/10.1085/jgp.58.6.667
53. Gracheva, M. E., Melnikov, D. V., & Leburton, J.-P. (2008). Multilayered semiconductor membranes for nanopore ionic conductance modulation. *ACS Nano, 2*(11), 2349–2355. https://doi.org/10.1021/nn8004679
54. Cory, S. M., Liu, Y., & Glavinović, M. I. (2007). Interfacial interactions of glutamate, water and ions with carbon nanopore evaluated by molecular dynamics simulations. *Biochimica et biophysica acta, 1768*(9), 2319–2341. https://doi.org/10.1016/j.bbamem.2007.06.006
55. Mao, M., Ghosal, S., & Hu, G. (2013). Hydrodynamic flow in the vicinity of a nanopore induced by an applied voltage. *Nanotechnology, 24*(24), 245202. https://doi.org/10.1088/0957-4484/24/24/245202
56. Hille, B. (2001). *Ionic Channels of Excitable Membranes* (3rd ed.). Sinauer Associates Inc.